

Impacts of Soil Heating Condition on Precipitation Simulations in the Weather Research and Forecasting Model

XINGANG FAN

Geosystems Research Institute, Mississippi State University, Starkville, Mississippi

(Manuscript received 13 June 2008, in final form 22 January 2009)

ABSTRACT

Soil temperature is a major variable in land surface models, representing soil energy status, storage, and transfer. It serves as an important factor indicating the underlying surface heating condition for weather and climate forecasts. This study utilizes the Weather Research and Forecasting (WRF) model to study the impacts of changes to the surface heating condition, derived from soil temperature observations, on regional weather simulations. Large cold biases are found in the 40-yr European Centre for Medium-Range Weather Forecasts (ECMWF) Re-Analysis project (ERA-40) soil temperatures as compared to observations. At the same time, a warm bias is found in the lower boundary assumption adopted by the Noah land surface model. In six heavy rain cases studied herein, observed soil temperatures are used to initialize the land surface model and to provide a lower boundary condition at the bottom of the model soil layer. By analyzing the impacts from the incorporation of observed soil temperatures, the following major conclusions are drawn: 1) A consistent increase in the ground heat flux is found during the day, when the observed soil temperatures are used to correct the cold bias present in ERA-40. Soil temperature changes introduced at the initial time maintain positive values but gradually decrease in magnitude with time. Sensible and latent heat fluxes and the moisture flux experience an increase during the first 6 h. 2) An increase in soil temperature impacts the air temperature through surface exchange, and near-surface moisture through evaporation. During the first two days, an increase in air temperature is seen across the region from the surface up to about 800 hPa (~1450 m). The maximum near-surface air temperature increase is found to be, averaged over all cases, 0.5 K on the first day and 0.3 K on the second day. 3) The strength of the low-level jet is affected by the changes described above and also by the consequent changes in horizontal gradients of pressure and thermal fields. Thus, the three-dimensional circulation is affected, in addition to changes seen in the humidity and thermal fields and the locations and intensities of precipitating systems. 4) Overall results indicate that the incorporation of observed soil temperatures introduces a persistent soil heating condition that is favorable to convective development and, consequently, improves the simulation of precipitation.

1. Introduction

The temperature and moisture conditions of the ground surface and shallow soil layers play an important role in influencing the evolution of weather and climate by providing a lower boundary condition to the atmosphere (e.g., Mintz 1984; Shukla and Mintz 1982; Mahfouf et al. 1987; Avissar and Pielke 1989; Chen and Avissar 1994; Sellers et al. 1997; Koster et al. 2004). This lower boundary condition is impacted by solar radiation, which heats the ground surface and thereby transfers

both sensible heat (via direct heating of the soil) and latent heat (via soil moisture evaporation and vegetation transpiration) to the overlying atmosphere. The partitioning of the available energy among sensible, latent, and ground heat fluxes depends on many variables, such as soil moisture (Pielke 2001; Sutton et al. 2006), roughness length (Diak et al. 1986), soil textural characteristics (Ek and Cuenca 1994), and vegetation characteristics (Xue et al. 1991). Errors in assessment of the state of the land surface may negatively impact subsequent weather forecasts. However, the sensitivity of land surface processes to the soil heating from upward ground heat flux, and consequently the impact on regional weather forecasts, is not well known.

Numerical land surface modeling has been an important area of research within the realm of weather and

Corresponding author address: Xingang Fan, Geosystems Research Institute, Mississippi State University, P.O. Box 2669, Starkville, MS 39762.
E-mail: fan@gri.msstate.edu

climate modeling, in order to prescribe as accurately as possible a ground surface condition with energy, mass, and momentum fluxes. The development of land surface models (LSM) has gone through various stages, evolving from simple parameterizations (e.g., Deardorff 1978; Entekhabi and Eagleson 1989) to complex soil–vegetation–atmosphere interaction models (e.g., Dai et al. 2003; Chen and Dudhia 2001). Among these LSMs, the community land model (CLM; Dai et al. 2003) is incorporated into the National Center for Atmospheric Research (NCAR) community climate system model (CCSM), widely used in climate studies. For mesoscale weather modeling, on the other hand, the so-called Noah land surface model (Chen and Dudhia 2001) was developed through the extension of the Oregon State University LSM (Pan and Mahrt 1987; Chen et al. 1996). The Noah LSM has been incorporated into the widely used fifth-generation Penn State University–NCAR mesoscale model (MM5; Chen and Dudhia 2001) and the Weather Research and Forecasting (WRF) model (Skamarock et al. 2005).

The continual advancement of LSMs has significantly improved the description of land surface conditions, which has consequently led to the improvement of numerical weather and climate predictions (e.g., Betts et al. 1997; Xue et al. 2001). However, as LSMs become increasingly complicated, additional uncertainties are introduced into modeling systems because of the insufficiency of available observations. Many of the newly introduced variables have to be determined on the basis of empirical relations or assumptions. For example, the Noah LSM assumes a constant-temperature lower-boundary condition, located by default at 3-m depth and assigned as the annual mean surface air temperature (Chen and Dudhia 2001), whereas CLM assumes the lowest boundary to have zero heat flux, although the total soil depth can be configured to be deeper than in Noah (Dai et al. 2003). As will be shown below, these assumptions are sometimes unrealistic and in sharp contrast to the true soil state.

Many observation-based diagnostic studies have revealed that there is a nonnegligible vertical heat flow between soil layers from depths of 0 to 3.2 m, as well as within the deep earth (e.g., Fan and Tang 1996; Harris and Chapman 1997; Pollack et al. 1998). Generally, conditions at deeper soil depths influence weather and climate at longer time scales. Likewise, information in shallower soil layers influences the atmosphere at shorter time scales (e.g., Huang et al. 1996). However, it is still not well understood how surface temperature change is transferred to deeper soil layers and how this energy is released at a later time, in combination with the deep soil energy of the inner earth, to subsequently

impact weather and climate. The observation data used in these studies include, in addition to deep borehole temperatures (e.g., Lachenbruch and Marshall 1986; Wang and Lewis 1992), meteorological station–observed soil temperatures that have been measured over the Eurasian continent for more than half a century, primarily from the former Soviet Union, Mongolia, and China. Figure 1 shows the distribution of such stations in Mongolia and China that observe soil temperature. Observation depths include 0, 0.05, 0.1, 0.15, 0.2, 0.4, 0.8, 1.6, and 3.2 m, which encompass the range of soil layers present in the Noah LSM and CLM default configurations. Such soil temperature data has been used in global climate change studies (e.g., Zhang et al. 2001, 2003; Chudinova et al. 2006) and diagnostic weather studies, from which it has been revealed that changes in soil temperature have predictive value for weather (Fan 1993, hereafter F93) and climate (e.g., Xin 1985; Tang et al. 1997). However, such soil temperature data has not yet been fully utilized in numerical weather and climate modeling.

In mesoscale weather simulations, soil temperatures are usually initialized by either ingesting global model forecasts or using data from reanalysis datasets. This study uses data from the 40-yr European Centre for Medium-Range Weather Forecasts (ECMWF) Re-Analysis project (ERA-40), which has a uniform horizontal grid spacing of 1.125° . In ERA-40's land surface parameterization scheme, the soil heat and water budgets are represented by two partial differential equations (Viterbo and Beljaars 1995). Solutions are based on the top and bottom boundary conditions: the net surface heat flux and precipitation minus evaporation are used for the top, while zero heat flux and free drainage assumptions are used for the bottom. Soil temperature follows a heat conduction equation, where the conductivity depends on soil water content, taken from the soil moisture initialization and short-range precipitation and evaporation forecasts. No observed soil temperature or moisture data is incorporated in the ERA-40 model.

Figure 2a shows the initial temperature of the second soil layer (0.1–0.4 m) in the Noah LSM, initialized from ERA-40 data, while Fig. 2b shows an analysis of observed soil temperatures vertically interpolated to 0.25 m, the midlayer depth of this model layer; their difference is shown in Fig. 2c. Even though the Cressman (1959) interpolated soil temperature shows some artifacts along the large domain boundaries because of sparse observation locations, the region of interest (especially the analysis box in Fig. 1) contains dense observations and the spatial structure of the heating field has an impact on heavy precipitation

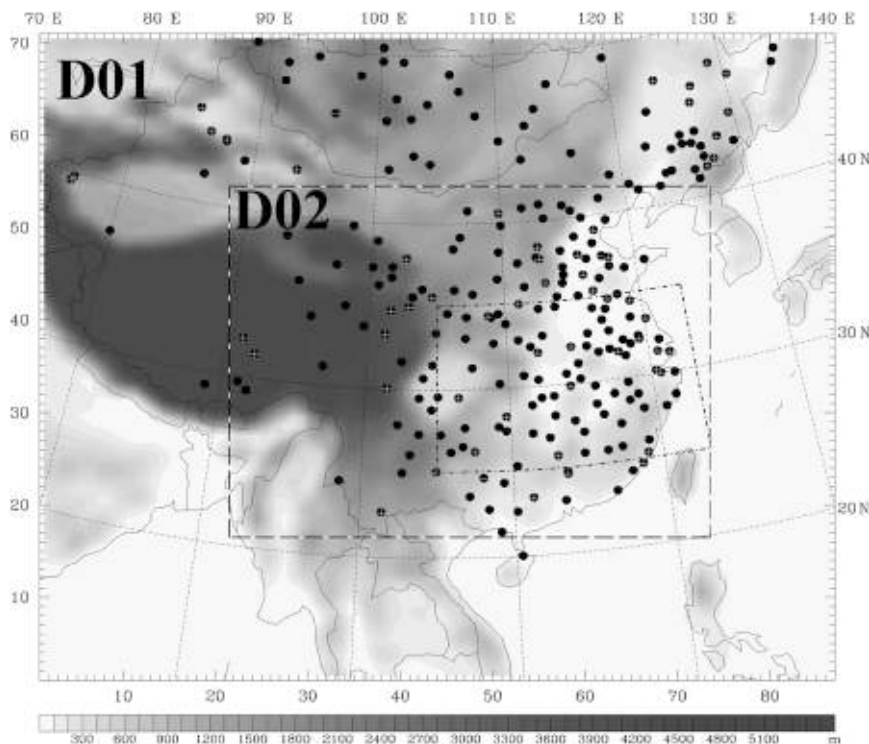


FIG. 1. Model domains with shaded terrain height and soil temperature observation sites. The dot-dashed latitude–longitude box, bounding the area 25°–35°N, 105°–123°E, is the analysis box described in the text.

(F93). We will therefore focus our analysis on the small domain (D02 in Figs. 1 and 2c). From the difference field, we see that the observed soil temperature depicts, on average, warmer soil in the second model layer, indicating that ERA-40 has an overall cold bias. This bias also exists in the other three soil layers (not shown), though the first (top) thin soil layer (0–0.1 m) temperature is largely dominated by the diurnal change in atmospheric temperature. Figure 3a shows the Noah LSM model-prescribed temperature at a depth of 3 m (the lower boundary), which is equated to the annual mean surface air temperature by default, while Fig. 3b shows an analysis of observed soil temperatures vertically interpolated to a depth of 3 m; Fig. 3c shows their difference. In the small domain (D02 in Fig. 3c), the default temperature is too warm in the west and too cold in the east. Because of the use of surface air temperature as a proxy for deep soil temperature, this difference is correlated with terrain height (see Fig. 1).

The question now becomes whether these differences in the initial soil temperatures, and in the conditions at the lower boundary, will be large enough to substantially impact the location, timing, and intensity of convection in mesoscale numerical simulations. Cheng and

Steenburgh (2005) suggested that improvements in LSM initialization may be just as, or more, important as improvements in LSM physics, and that efforts must be undertaken to improve both LSM initialization and the parameterization of coupled land surface–boundary layer processes in order to produce more accurate surface sensible weather forecasts. Considering the presence of bidirectional heat transfer within soil, a realistic treatment of the lower boundary condition of an LSM thus becomes highly important in land surface, weather, and climate simulations.

Following on to the diagnostic findings from F93, in this study the latest version (at the time of this study) of the mesoscale atmospheric model Advanced Research WRF (ARW) and one of its popular land surface components, Noah LSM, are initialized with actual observations of soil temperature to investigate the degree to which shallow layer soil heating conditions impact surface fluxes, atmospheric boundary layer properties, and weather simulations. Model initialization using such soil temperature observations is studied for the first time. Section 2 describes the model setup, data utilization, and experiment design. Section 3 summarizes the diagnostic findings of F93 and the synoptic background of the cases chosen for this study. Section 4

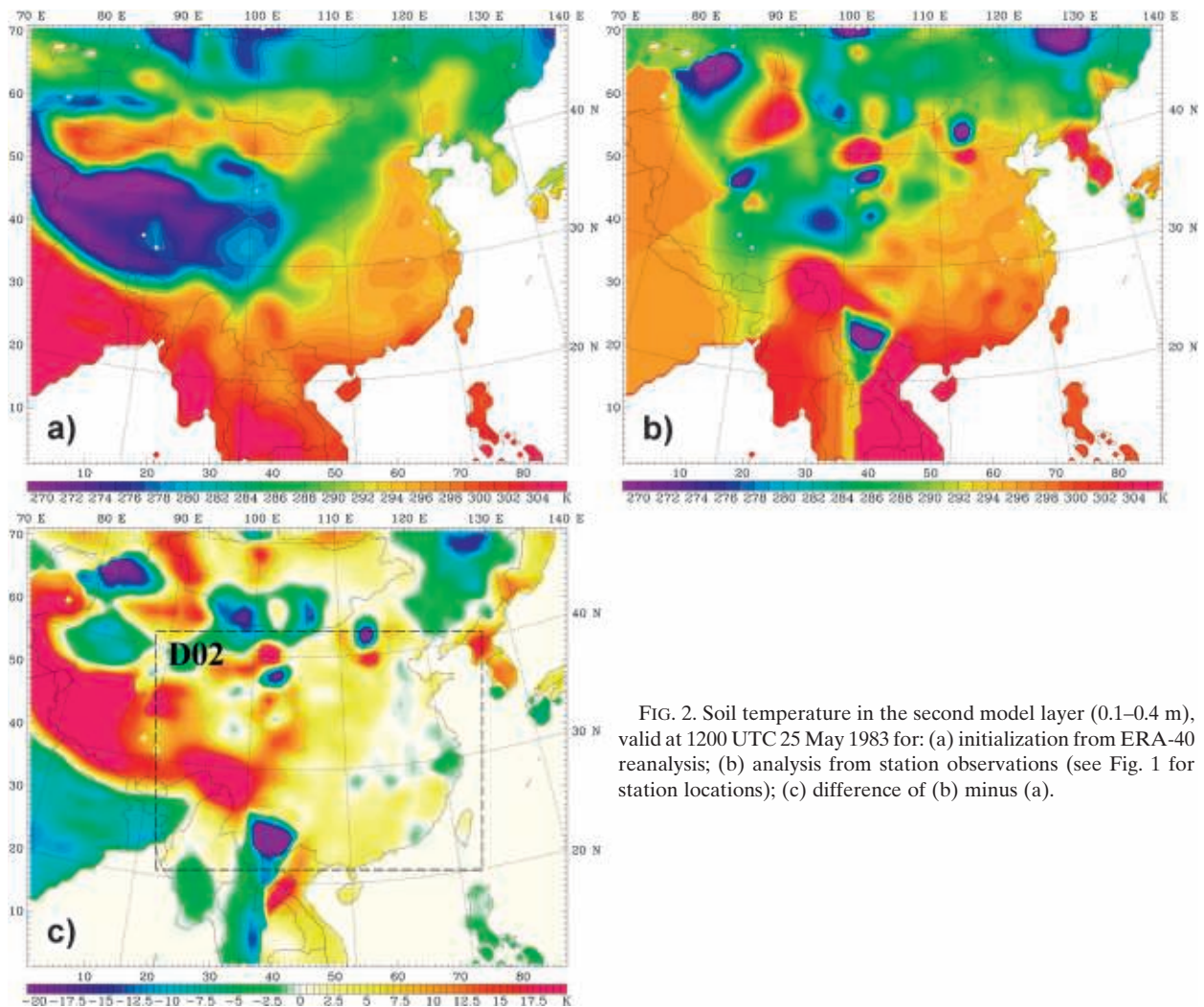


FIG. 2. Soil temperature in the second model layer (0.1–0.4 m), valid at 1200 UTC 25 May 1983 for: (a) initialization from ERA-40 reanalysis; (b) analysis from station observations (see Fig. 1 for station locations); (c) difference of (b) minus (a).

analyzes and discusses the results. Section 5 summarizes the conclusions.

2. Model setup, data preparation, and experiment design

The Advanced Research WRF, version 2.2, and its Noah LSM component were used to simulate selected cases and investigate the impacts of the utilization of observed soil temperatures. The observations are sufficient to provide regional initialization of soil temperatures at four model layers, as well as for providing lower soil boundary conditions. The WRF model has proven to be advantageous for sensitivity studies and inter-model comparisons (Cheng and Steenburgh 2005), and the current version produces comparable results to those of the final version of MM5 (version 3.7) in simulating extreme wind events (Fan et al. 2007).

a. WRF model setup

The WRF model is configured with two one-way nested domains with 60-km grid spacing (86×71 grid points) over East Asia and 20-km spacing (157×115 grid points) centered on the midpoint of the Yangtze River. As mentioned in section 1, the emphasis here is on the fine resolution domain (nest D02). The configuration has 49 vertical terrain-following eta levels, with increased vertical resolution in the lower levels. The eta intervals increase from 0.002 at the surface to 0.02 at model top, corresponding to height intervals of ~ 8 m at the bottom to ~ 888 m at the top. The following physics packages are used: WRF single-moment (WSM) 5-class cloud microphysics scheme (Hong et al. 2004), Rapid Radiative Transfer Model (RRTM) longwave radiation scheme (Mlawer et al. 1997), Dudhia (1989) shortwave radiation scheme, Mellor–Yamada–Janjic TKE

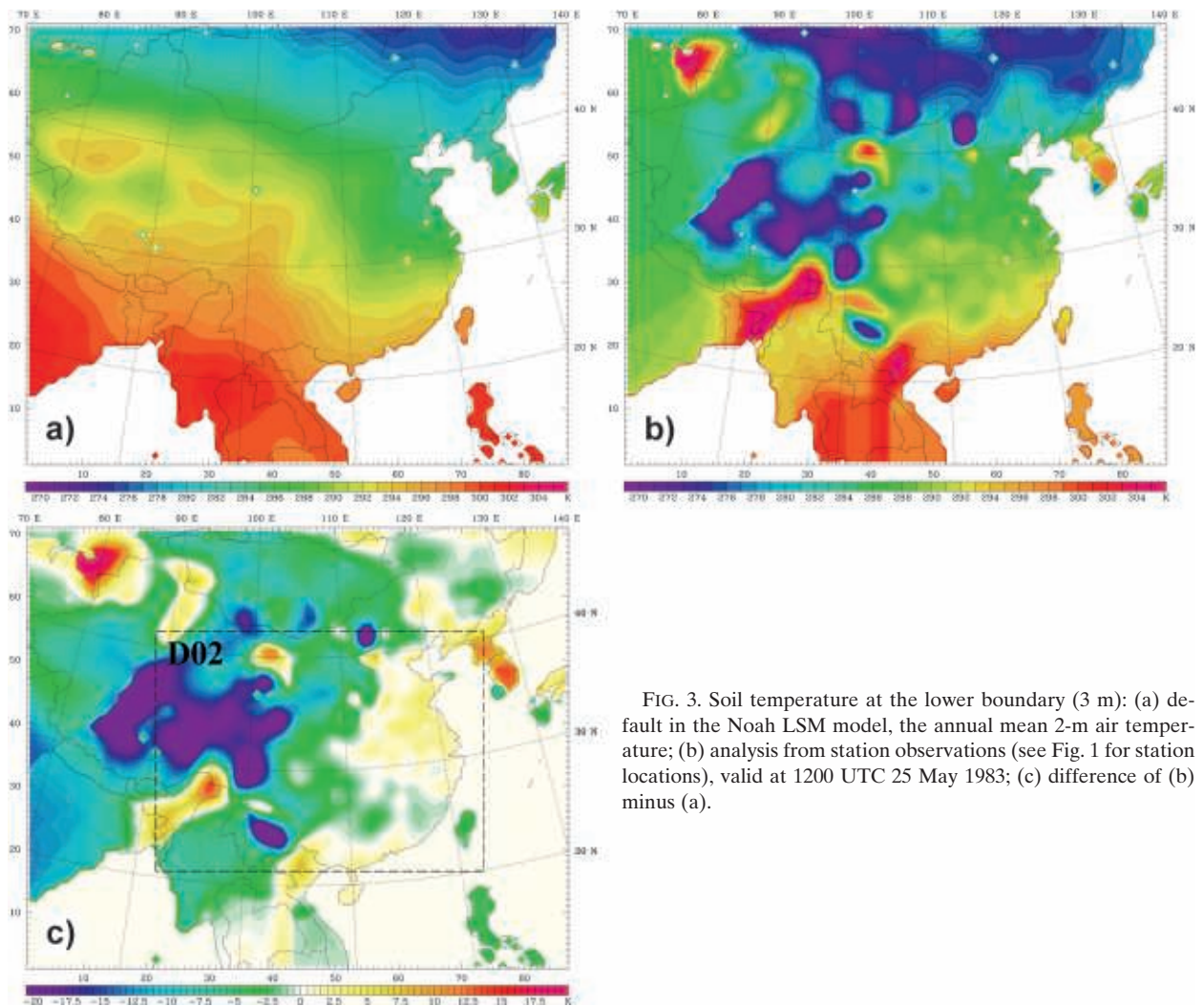


FIG. 3. Soil temperature at the lower boundary (3 m): (a) default in the Noah LSM model, the annual mean 2-m air temperature; (b) analysis from station observations (see Fig. 1 for station locations), valid at 1200 UTC 25 May 1983; (c) difference of (b) minus (a).

boundary layer scheme (Janjic 1996, 2002), Noah LSM (Chen and Dudhia 2001), and Grell–Devenyi ensemble cumulus parameterization (Grell and Devenyi 2002).

In the Noah LSM, four soil layers are specified with depths of 0–0.1, 0.1–0.4, 0.4–1.0, and 1.0–2.0 m, with midlayer depths at 0.05, 0.25, 0.7, and 1.5 m, respectively. The lower boundary is set to a depth of 3 m.

b. Data

ERA-40 reanalysis data is used to drive the WRF model by providing initial and boundary conditions. Soil temperature and moisture data are available for the layers 0–0.07, 0.07–0.28, 0.28–1.0, and 1.0–2.55 m in this dataset, which are then interpolated to the model soil layers by the WRF preprocessor in order to provide soil temperature and moisture initialization.

A set of monthly soil temperature data from China and Mongolia (e.g., Tang and Zhang 1994; Fan and

Tang 1996) was used to provide observed initial soil temperature and lower soil boundary conditions. These data are located at depths of 0, 0.2, 0.4, 0.8, 1.6, and 3.2 m (the top level is the skin temperature), with the raw observations made 4 times per day at 0–0.4 m using a bent-stem thermometer, and once per day (0600 UTC) at 0.8–3.2 m using extraction thermometers, both with an accuracy of 0.1°C. F93 used daily soil temperatures that were digitized from the Monthly Meteorological Report (Climate Data Office 1981, 1984) solely for rainfall regions over short time periods. For this study, the monthly data is the only available source of soil temperatures present across the entire model domain. Because of the unavailability of daily soil temperature data in these datasets, the monthly data were linearly interpolated in time in order to obtain the 6-hourly soil temperatures. As shown in section 4b, the monthly data provide the general trend for the soil temperatures in the bottom three layers, as well as the lower boundary.

The first (top) layer is primarily influenced by daily atmospheric conditions and solar insolation. The model's adjustment of the top soil layer is very fast (less than three hours; see Fig. 7) relative to the bottom three layers. Thus, the soil temperature data used here provide sufficient information to the modeling system. The modeling results indicate that the daily average top-layer soil temperatures are approximately close to those at 0300 UTC (1100 LT) and 1500 UTC (2300 LT). Therefore, initializing the coarse domain at 0000 UTC and the fine domain at 1200 UTC is reasonable, considering that the ERA-40 reanalysis data is only available at 0000, 0600, 1200, and 1800 UTC. To utilize the observed soil temperature data within the Noah LSM, a similar procedure to that used by the WRF preprocessor was applied. The soil temperature observations were first interpolated to a $0.5^\circ \times 0.5^\circ$ grid through the use of multiple passes of the Cressman (1959) scheme, and then interpolated to depths of 0.05, 0.25, 0.7, and 1.5 m, the midlayer depths of the four model soil layers. Data interpolated to 3 m were utilized as the Noah LSM lower boundary condition. Since the observed data were introduced at the preprocessing stage, they were used in the same manner as the ERA-40 soil temperature data.

Considering that the daily data used in this study were linearly interpolated from monthly means, an analysis of the modeled soil temperature diurnal change was conducted. The maximum diurnal variation for all stations within domain D02 at the four soil layers (top down) were 15.2° , 3.2° , 0.8° , and 0.4°C , respectively. As mentioned above, the temporal linear interpolations were at most 3 h off when used to initialize the model. Thus, the error in the initializing soil temperature data is approximately within 3.8° , 0.8° , 0.2° , and 0.1°C at the four layers, respectively. As we see from Figs. 2 and 3, the differences between ERA-40 and the observations are much greater than the maximum error of the above rough estimate.

c. Experiment design

In a weather model, though the cumulus parameterization scheme (CPS) is one factor that can significantly impact precipitation forecasts, many other important factors also exist. The improvement of model initial conditions is crucial for reducing errors in precipitation forecasts (Cheng and Steenburgh 2005), and is the focus of this article.

Wang and Seaman (1997) compared the performance of four different CPSs within the MM5 model by simulating six heavy rain events. One major conclusion they drew was that all four CPSs produce reasonably accurate forecasts of total precipitation volume, considered a key forecast variable and an important indicator of a successful forecast. In this study, changing initial soil tem-

perature affected both total sensible and latent heating, which in turn caused differences in total volumetric precipitation, reflecting the total amount of latent heating produced by the model (Wang and Seaman 1997). For simplicity, the experiments here were designed to have only one factor changed—the soil temperature.

Two sets of numerical simulations were conducted in which two different data sources were used for the soil temperature initialization and lower boundary conditions. The control simulation (CTRL) used the ERA-40 soil temperatures (Fig. 2a) and the default WRF lower boundary condition (Fig. 3a). The experimental simulation (OBST) used the observed soil temperatures (Figs. 2b and 3b) for both initialization and the lower boundary condition.

To allow the model to have sufficient time to respond to the change in soil conditions, the simulation period was set to 5.5 days, spanning 3.5 days prior to the heavy rain day, the rain day, as well as one following it. Since the nested fine domain is emphasized in the analysis, an additional 12 h were simulated on the coarse domain prior to the initialization of the nest so that the initial and boundary conditions provided to the nest were sufficiently spun up. Note that the soil temperature data used for the nested domain were directly read in from files. The analysis of the modeling results begins from simulation hour 18 (note: the simulation hour is relative to the initial time of the coarse domain) in order to leave a 6-h spinup period for the nest. The simulation and analysis time periods for each of the six chosen cases (see next section) are listed in Table 1. This setup was constructed taking into account the diagnostic results from F93 that soil temperature patterns are maintained for about 3–4 days prior to the onset of heavy precipitation.

3. Diagnostic facts and case selection

In F93, 19 torrential rain events that occurred in the mid-to-lower reaches of the Yangtze River basin in China in the years 1980 and 1983 were analyzed. Seventeen of the cases produced daily precipitation accumulations at individual stations in excess of 100 mm, while the other two saw maximum totals from 75 to 100 mm. Note that the maximum daily rainfall from different data sources may contain subtle differences, depending on the availability of stations that are included in each dataset. F93 used data taken directly from the reports of meteorological stations that are located within the analysis box shown in Fig. 1, while in this article the National Climatic Data Center's global surface summary of daily rainfall data was instead used for the entire domain. In F93, shallow layer soil heating was derived from the daily temperatures of two soil

TABLE 1. Simulation and analysis time periods of the six chosen cases (Dates are in the form of year (yyyy)-month (mm)-day (dd) hour (hhhh) or mm-dd hhhh UTC).

Case No.	Initial time		Analysis	Rain day	End time
	Coarse domain	Fine domain			
1	1980-07-05 1200	07-06 0000	07-06 0600	07-09 0000 ~ 07-10 0000	07-11 0000
2	1980-07-16 1200	07-17 0000	07-17 0600	07-20 0000 ~ 07-21 0000	07-22 0000
3	1980-08-08 1200	08-09 0000	08-09 0600	08-12 0000 ~ 08-13 0000	08-14 0000
4	1983-05-25 1200	05-26 0000	05-26 0600	05-29 0000 ~ 05-30 0000	05-31 0000
5	1983-06-11 1200	06-12 0000	06-12 0600	06-15 0000 ~ 06-16 0000	06-17 0000
6	1983-06-26 1200	06-27 0000	06-27 0600	06-30 0000 ~ 07-01 0000	07-02 0000
Model hour	0	12	18	84 ~ 108	132

levels (0.2 and 0.8 m; 0.4 m data was used where either the 0.2 or 0.8 m data was missing). This was done by first calculating the soil temperature anomalies, denoted as $T'_{0.2}$, $T'_{0.4}$, and $T'_{0.8}$, by subtracting the long-term daily mean from the daily data. The daily mean was obtained by interpolating the long-term monthly mean of 30–40 yr of monthly data linearly in time. The difference $T'_{0.8} - T'_{0.2}$ was then calculated and denoted as the shallow layer soil heating index (SHI). A positive value of SHI indicates a larger than normal upward (or smaller than normal downward) heat flow within the soil layer.

Two types of relationships between SHI and rainfall were distinguished in F93. In a type 1 relationship, it was found that the axis of a positive SHI area is coincident with the axis of rainfall area when the low-level (850 hPa) horizontal wind shear runs parallel to the SHI axis. Usually, the distance between the rainfall and SHI axes in these cases is less than 100 km. In a type 2 relationship, when the low-level horizontal wind shear crosses the positive SHI axis, the rain usually falls on the downwind side of the SHI axis, while the axis of rainfall area is approximately parallel to the SHI axis and the distance between the two axes is usually in the range of 100–400 km. The duration of a formed positive SHI area for torrential rain events is about 4–7 days and is initiated roughly 3–4 days before the event. Thus, the SHI field, in combination with existing weather patterns, impacts the development of rain systems and predicts the location of rain.

In this study, six type 1 cases from F93 were chosen for further investigation, in part because of the simplicity of the associated weather patterns, and also because type 1 occurred more frequently than type 2 (14 vs. 5). The soil temperature patterns in these cases were maintained relatively longer and the rainfall areas were larger than in the others. Table 1 lists the selected cases and the simulation and analysis time periods, which are explained in section 2c.

This article presents the averaged results from all six cases while the fourth case, 25–31 May 1983, is used for illustration. Figure 4a shows the daily total precipi-

tation distribution on 29 May 1983 (ending at 0000 UTC 30 May 1983) for the area bounded by the fine domain; Fig. 4b shows the sea level pressure, surface air temperature, and surface wind barbs of the CTRL run valid at 1800 UTC 29 May 1983. There were two low pressure systems aligned along the 30°N parallel, each maintained for about one day, and the heavy rain was caused by the surface quasi-stationary frontal system, accompanied by southwest wind at the surface and a low-level jet at 850 hPa (cf. Fig. 14a). The axis of the rain zone is largely parallel to the fronts.

In addition to the correction of the cold bias in the ERA-40 soil temperatures by the observed data, the utilization of observed soil temperatures is expected to incorporate the observed SHI features into the modeling study. SHI, as defined in F93, is the vertical soil temperature gradient anomaly between 0.2 and 0.8 m. In F93, the axis of positive SHI area for the 25–31 May 1983 case was shown to also be aligned along the 30°N parallel, where the low pressure systems were located. In this study, however, the actual soil temperature, instead of its anomaly, is used. Therefore, the soil heating features need to be analyzed from the soil temperature itself. Figures 5a,c,e show, for the initial time of the fine domain in the OBST run, the differences in the vertical soil temperature gradient between observed and ERA-40 soil temperatures. Since the model soil-layer thicknesses are constant, the soil temperature difference between two adjacent layers is used as a proxy for the gradient. Among the four model layers, layers 2 and 3 are closest to what was used in F93, because the midlayer depths of these two are 0.25 and 0.7 m, respectively. Assuming the same long-term mean for both ERA-40 and observed data, the difference fields of the vertical gradient shown in Fig. 5c would imply the difference in SHI between the two datasets. In Fig. 5c, an increase of the vertical soil temperature gradient is seen in the observations relative to ERA-40. Namely, a positive SHI area is implied in the observations and is aligned along the 30°N parallel. Comparing Figs. 5a and 5e with Fig. 5c, this soil heating feature exists at all three layers

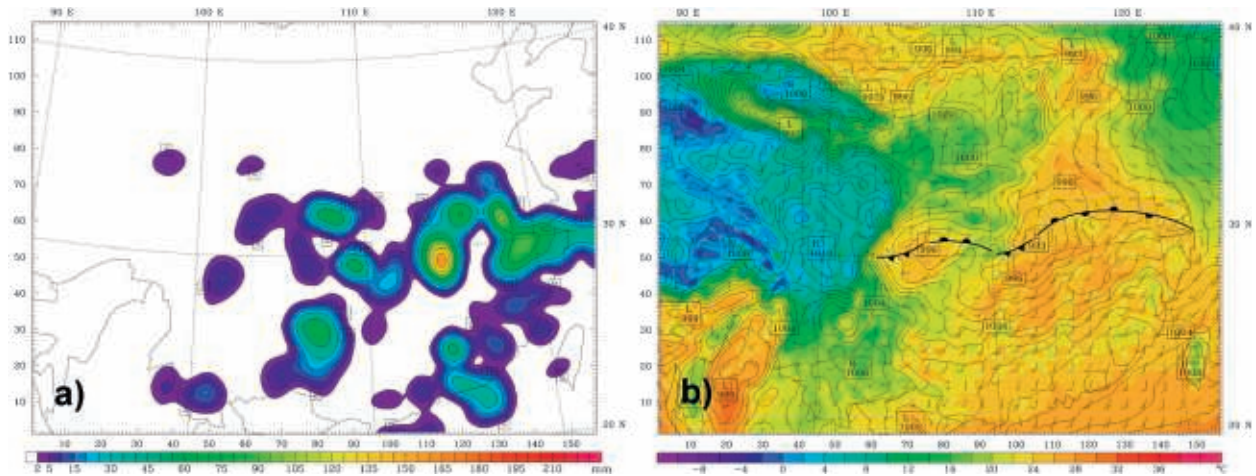


FIG. 4. (a) Analysis of station-observed 24-h accumulated precipitation totals (mm), valid at 0000 UTC 30 May 1983; (b) Sea level pressure (1-hPa contour interval), surface air temperature (color), and surface wind barbs (full barb is 5 m s^{-1}) of the CTRL run, valid at 1800 UTC 29 May 1983.

and is stronger at lower layers. This also implies that the lower boundary condition is important to the LSM.

4. Modeling results and analysis

The cases studied herein all occurred in the mid-to-lower reaches of the Yangtze River basin, the same region studied in F93. The modeling analysis here also focuses on this region as shown in Fig. 1; that is, the latitude–longitude box bounded by 25° – 35° N, 105° – 123° E. For verifications conducted at station locations, the closest model grid point to each station is used for comparisons and/or calculations. The smallest distance between two stations within the analysis box is about 54 km, while the average station-to-station distance is about 106 km. Thus, for station verification on the fine domain (20-km grid spacing) there is no repeated use of station or model data. For statistical analysis within the designated box, all available stations and their corresponding model grid points are used. The total number of stations used in the analysis ranges from 198 to 213 over the six cases. For the precipitation skill scores, a gridded analysis of observations is used in order to better capture the spatial distribution of precipitation in the analysis box, further explained in section 4a.

a. Precipitation

A common phenomenon among all the study cases was a period of heavy rain that occurred during the fourth day of simulation, between simulation hours 84 and 108. Figures 6a,b show 24-h accumulated precipitation from the experiments OBST and CTRL, respectively, valid at 0000 UTC 30 May 1983. The CTRL experiment produced a broader rain area than was ob-

served, with a maximum rainfall of 82.5 mm, much less than the observed maximum (163.5 mm). In comparison, the OBST experiment produced a similar rain area as that seen in CTRL. However, the rainfall is more intense; it reaches a maximum of 98.2 mm. The rainfall center along the eastern coast also increased from 49.6 mm in CTRL to 94.2 mm in OBST. Figure 6c shows the differences in accumulations between the two experiments to give an overall view of the impacts on precipitation. The precipitating systems west of 118° E systematically shifted to the southeast in OBST. This is consistent with the persistent mesoscale feature of increased spatial variability in the soil temperature in OBST (see discussions in section 4b). There is also a systematic increase in the rainfall amounts along the fronts and the observed rain zone. Maximum increases of 54.0 and 61.7 mm occurred in the primary rain center and the eastern coastal rain center (Fig. 6c), respectively. These increases are not collocated with the centers of maximum rain and include the effects from changes in both the strength and location of the rain centers. The magnitude of the change in rain strength is approximately equal to the difference in maximum precipitation between the two experiments. The change related to location can be estimated by subtracting the strength-related change from the amount of maximum increase.

To study the regional average and the timing of the precipitation, the modeled 3-hourly accumulated precipitation is averaged over all the stations (using closest grid points) within the analysis box. Two time series of regionally averaged three-hourly precipitation from the CTRL and OBST experiments are shown in Fig. 7 (bottom panel). Significant differences in regional average

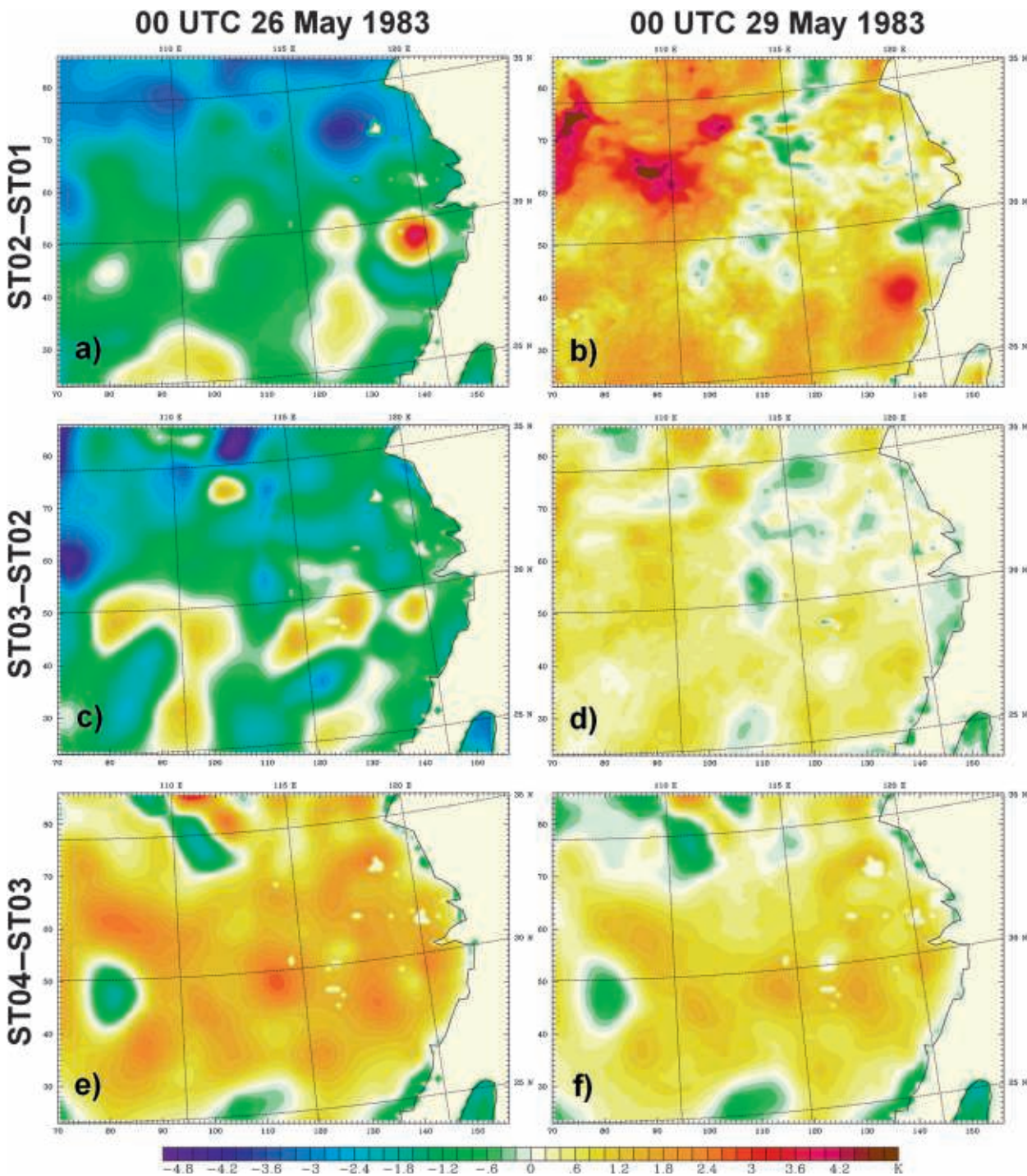


FIG. 5. Difference between the OBST and CTRL experiments for the vertical soil temperature gradient, in the form of the difference between two adjacent layers, (a),(b) ST02 – ST01, (c),(d) ST03 – ST02, and (e),(f) ST04 – ST03, valid at (a),(c),(e) 0000 UTC 26 May 1983 and (b),(d),(f) 0000 UTC 29 May 1983.

precipitation between OBST and CTRL occurred on the third and fifth days. The third day showed a significant change in magnitude, while the fifth day showed a significant difference in timing. Both the OBST and

CTRL runs produced a similar amount of precipitation on the fourth day, which contained the heavy rain peak; however, such a regional average does not reflect the rainfall location changes shown in Fig. 6.

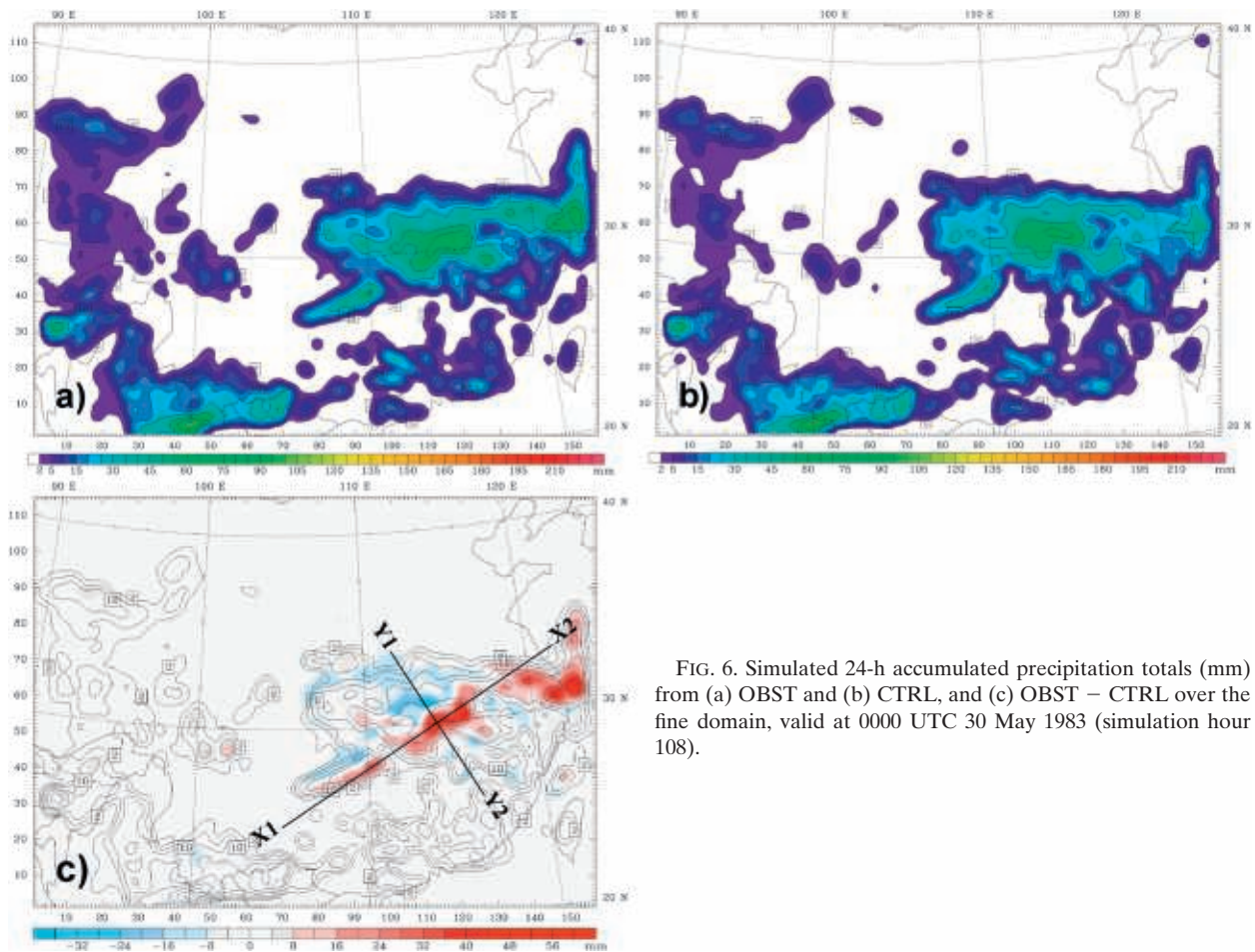


FIG. 6. Simulated 24-h accumulated precipitation totals (mm) from (a) OBST and (b) CTRL, and (c) OBST - CTRL over the fine domain, valid at 0000 UTC 30 May 1983 (simulation hour 108).

For the purpose of analyzing the development and/or the evolution of the precipitation system, Figs. 8 and 9 show the spatial distribution of the modeled 6-hourly accumulated convective rainfall and explicit (large scale) rainfall, respectively, from the two experiments and their differences on the fourth simulation day. Before the beginning (0000 UTC 29 May 1983) of the fourth day, there were only two small isolated rain centers along the 30°N parallel (not shown). Convective precipitation began within the first 6 h over a broad area (Figs. 8a,e) and continued to intensify during the second 6-h period (Figs. 8b,f). There was little explicit precipitation during the first half of the day (Figs. 9a,b,e,f). After 1200 UTC, the convective precipitation decreased in both areal coverage and intensity (Figs. 8c,d,g,h). Explicit precipitation slightly increased (Figs. 9c,d,g,h), though its intensity was still very small compared to the convective precipitation. The predominant precipitation area is along 30°N as clearly shown in Fig. 6. The differenced precipitation fields (OBST - CTRL) in Figs. 8 and 9 show an obvious increase along the 30°N parallel during the first 12 h. During the second 12-h

period, the adjacent large negative and positive changes indicate a southeastward shift of the precipitation. These changes are associated with the surface heating and large-scale weather pattern, which will be discussed in the following subsections.

To produce an objective and quantitative analysis, the equitable threat score (ETS) and categorical bias (Wilks 1995) have been calculated. ETS and bias measure the skill in predicting the frequency of precipitation that is equal to or greater than a given threshold. Higher ETS implies better forecasting skill. A bias equal to 1 signifies a perfect forecast of the precipitation frequency; greater than 1 implies an overestimate while less than 1 signifies an underestimate. Such verification of model performance is again focused on the entire analysis box used in this study. A gridded precipitation field, derived from the station observations within the analysis box, is used in calculating the ETS and bias scores. This is done to somewhat compensate for the relative sparsity of observations, and allows the spatial shifts and changes in the precipitation centers over the entire region of heavy rain between the two model simulations to be

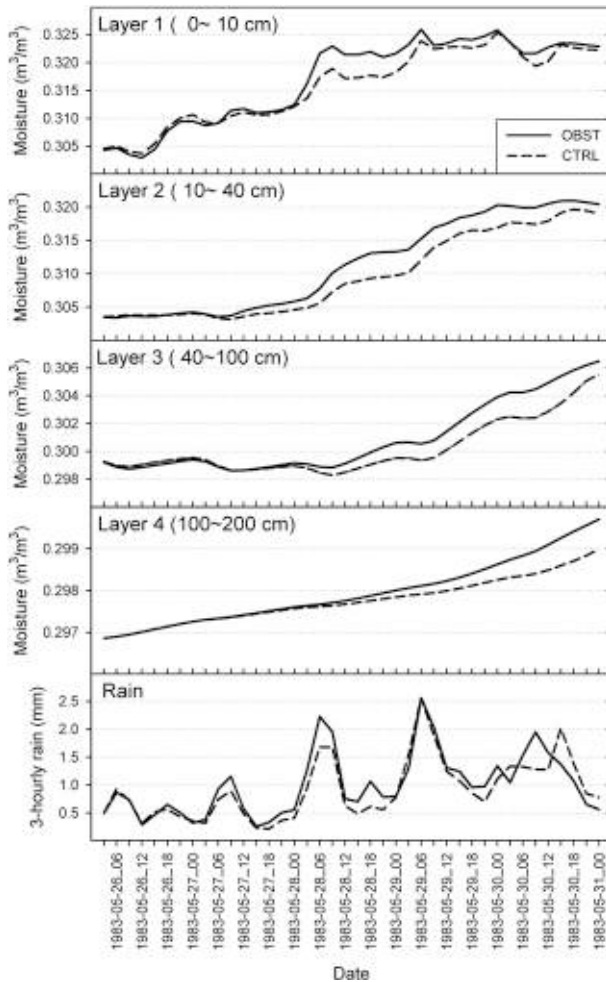


FIG. 7. Average of soil moistures ($\text{m}^3 \text{m}^{-3}$) from stations within the area $25^\circ\text{--}35^\circ\text{N}$, $105^\circ\text{--}123^\circ\text{E}$ in the four model soil layers, from OBST (solid) and CTRL (dashed). (bottom) Three-hourly accumulated precipitation totals (mm) from the two runs.

better captured. The ETS and bias scores for the 24-h accumulated precipitation on the fourth day of the CTRL and OBST experiments are calculated at thresholds of 2, 5, 10, 20, 30, 50, 75, and 100 mm. Results from the illustrative case (not shown) indicate that OBST has better skill and accuracy than CTRL in predicting large precipitation totals of greater than 20 mm. For the 5- and 10-mm thresholds, OBST is less skillful than CTRL, but the bias scores indicate that the prediction of overall frequency is improved in OBST.

The above impacts on precipitation resulted solely from the change in soil temperature initialization in the four soil layers and at the lower boundary, as described in section 2. The mechanism of how the changes in soil propagate to the land surface and atmosphere, and how they ultimately affect the precipitation, will be analyzed in the following subsections. Emphasis will also be placed

on the two cross sections X1–X2 and Y1–Y2 as shown in Fig. 6c.

b. Persistent impacts on soil temperature

The changes made at the initial time have been described in section 1 (see Figs. 2 and 3). How would these changes in soil temperature evolve as the model integrated for several days? Figure 10 shows the model soil temperature averaged over all stations (205 stations, using closest grid points) within the analysis box for the four soil layers, as well as for the lower boundary. In OBST, at the time of fine domain initialization, the average soil temperatures in each of the four model layers from top to bottom increased 5.1° , 3.7° , 2.5° , and 3.2°C , respectively, relative to CTRL; the average soil temperature at the lower boundary decreased 2.5°C . The top soil layer shows strong diurnal changes in temperature. The air and skin temperatures are warming at this time of year, and this feature is shown in both the CTRL and OBST experiments after an approximately 3-h spinup period. The initial time for the fine domain is 0800 LT (0000 UTC), when the temperature of the top soil layer is about to rise, but the warmer soil in OBST relative to CTRL experienced a spinup period to adjust to the relatively cold air. Therefore, a temperature drop is seen during the first 3-h period and, consequently, causes the reduced temperature difference between OBST and CTRL after the spinup. The discontinuity in soil temperature is also seen in all layers in CTRL. This is because the soil temperature initialization for the fine domain is read directly from input data rather than interpolated from the coarse domain as is done for many other variables. The soil temperature of the second layer features a weak diurnal variation. In addition, the adjustment in the second layer is rather slow compared to the top layer. The temperature decreased over the first two days and only then began to rise. This is because the adjustment of the top soil layer involves both radiative and latent energy exchange, while that of the second layer primarily involves conductive heat transfer, a slow and ineffective way of transferring energy. Temperatures of the third and fourth layers, on the other hand, exhibit very little diurnal change, though the overall warming trend is still evident. The lower boundary has been set to be invariant in the Noah LSM and for this study; however, the observed month-to-month change shows an increasing trend.

Despite these smoothly varying changes in the regional average soil temperatures, we see that these changes can vary quite a bit spatially (see Figs. 2 and 3). Essential questions are: how persistent will these changes be, how would these changes affect energy flows in the soil, and

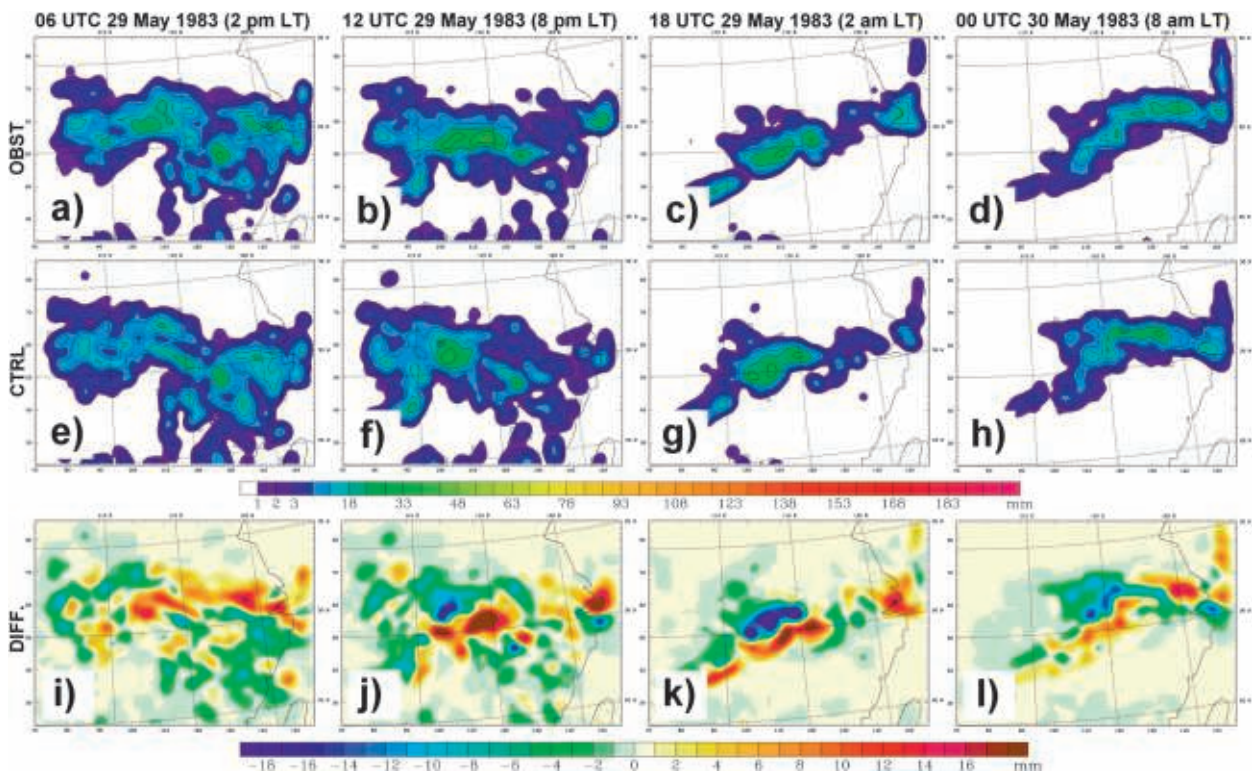


FIG. 8. The 6-h accumulated convective precipitation (mm) from experiments (a)–(d) OBST and (e)–(h) CTRL, and (i)–(l) their differences (DIFF = OBST – CTRL), valid at 0600, 1200, 1800 UTC 29 May and 0000 UTC 30 May 1983.

how would the changes in soil energy flow subsequently affect the surface and the air?

Soil energy flow is determined by the soil temperature gradient. Our focus here is on the change in the vertical temperature gradient, which is consequently associated with the change in energy flow. As discussed in section 3, soil temperature differences between adjacent layers can be used to represent the vertical gradient and, in particular, the difference between layers 3 and 2 implies the SHI used by F93. The differences in this gradient between OBST and CTRL at the beginning of the fourth simulation day are shown in Figs. 5b,d,f. Positive areas signify an increase in upward energy flow in OBST relative to CTRL. Comparing Figs. 5b,d,f to 5a,c,e, respectively, the features of the increased upward energy flow seen at the initial time continue to exist at the beginning of the fourth simulation day. Additionally, the upward energy flow is expanded over a larger area in the upper layers. Even though there are other areas outside of the heavy rain area that show increased upward energy flow, which might have impacts on surface and atmospheric parameters, this does not necessarily impact the precipitation because: 1) precipitation depends on the existing weather pattern and moisture conditions; and 2) the impacts on the precipitation as discussed in

section 4a are larger for convective precipitation than explicit, which implies a larger impact locally than at a larger scale. However, impacts from those areas might cause impacts on the large-scale flow patterns that affect the production of heavy rain, but again this effect should be small for the above reason 2.

Since the OBST soil contains higher soil temperatures (e.g., Figs. 2 and 10) and increased upward energy flow (Fig. 5) than in CTRL, while the atmosphere in both experiments is initialized from the same ERA-40 data, the soil provides stronger heat fluxes to the air in OBST than in CTRL. In other words, the top soil layers in OBST lose more energy compared to CTRL, which also explains the reduced warming trend seen in OBST (Fig. 10). As the soil state is slow to change, the features shown in Fig. 5 last for several days throughout the entire simulation period.

c. Impacts on soil moisture

Soil moisture is directly influenced by precipitation, soil temperature, surface wind, and evaporation. Although the impacts on soil moisture from each individual factor cannot be separated, here we emphasize the overall impacts that are inherited from the introduction of different soil temperature initializations in

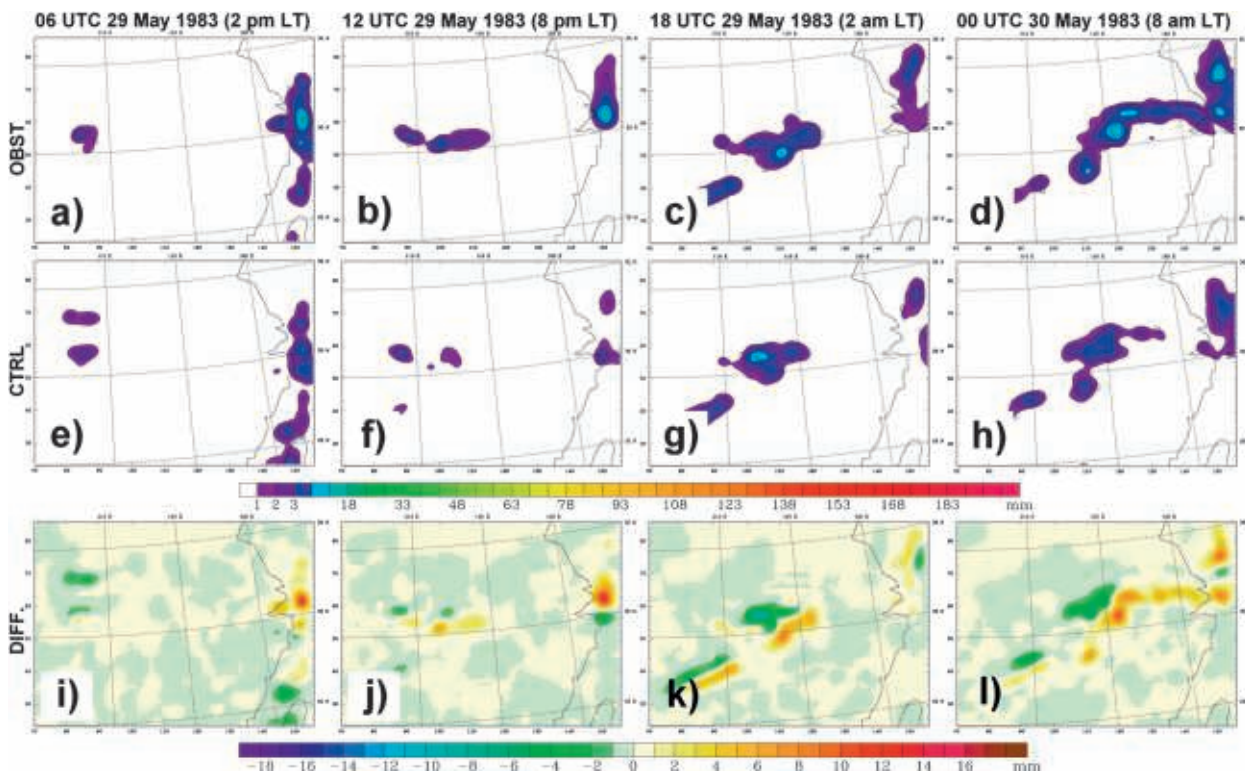


FIG. 9. The 6-h accumulated explicit precipitation (mm) from experiments (a)–(d) OBST and (e)–(h) CTRL, and (i)–(l) their differences (DIFF = OBST – CTRL), valid at 0600, 1200, 1800 UTC 29 May and 0000 UTC 30 May 1983.

the CTRL and OBST experiments. The soil moistures, averaged over all stations within the analysis box for the four soil layers, are shown in Fig. 7. It is shown that: 1) the two experiments produced significantly different soil moistures, especially from simulation day three on; 2) the soil moisture change is closely related to changes in precipitation. The top soil layer shows nearly coincidental changes in soil moisture to those seen in precipitation; 3) although changes in the soil moisture lag in the deeper layers, the changes do indeed propagate down through the soil. The moisture in the bottom soil layer began to show differences on the fourth day of simulation; and 4) the combined effects from the soil temperature change and a lack of significant rainfall during the first day of simulation caused a decrease in OBST soil moisture relative to CTRL. As discussed in the next subsection, the decrease in soil moisture in the top layer during the first day is associated with the increase in soil temperature as well as an increase in surface evaporation.

d. Impacts on ground and surface fluxes and on surface properties

As pointed out in the previous subsection, energy fluxes are the most essential variables to investigate in

order to understand the impacts of an observation-based soil temperature initialization. Figure 11 shows the average upward ground heat flux (Fig. 11a), surface upward sensible heat flux (Fig. 11b), and surface upward latent heat flux (Fig. 11c) within the analysis box from the CTRL and OBST experiments, and their differences between OBST and CTRL; that is, OBST minus CTRL.

Ground heat flux is defined as the heat transfer from the top soil layer to the ground surface, providing an energy source from the soil to the soil–atmosphere interface. Normally, there is a downward ground heat flux during the day and an upward heat flux at night, due primarily to the effects of short- and longwave radiation. In the cases simulated in this study, the daytime downward heat flux has a greater magnitude than the upward heat flux at night, because of the geographical region and time of year. Figure 11a indicates that the change in soil temperature as described in section 4b introduced a consistent positive difference in the ground heat flux in OBST relative to CTRL throughout the simulation period. Since the change is introduced only once, at the initial time, while atmospheric initial conditions and lateral boundary conditions remained the same as in CTRL, it is not surprising to see the impacts diminish over time. However, it is interesting to see that

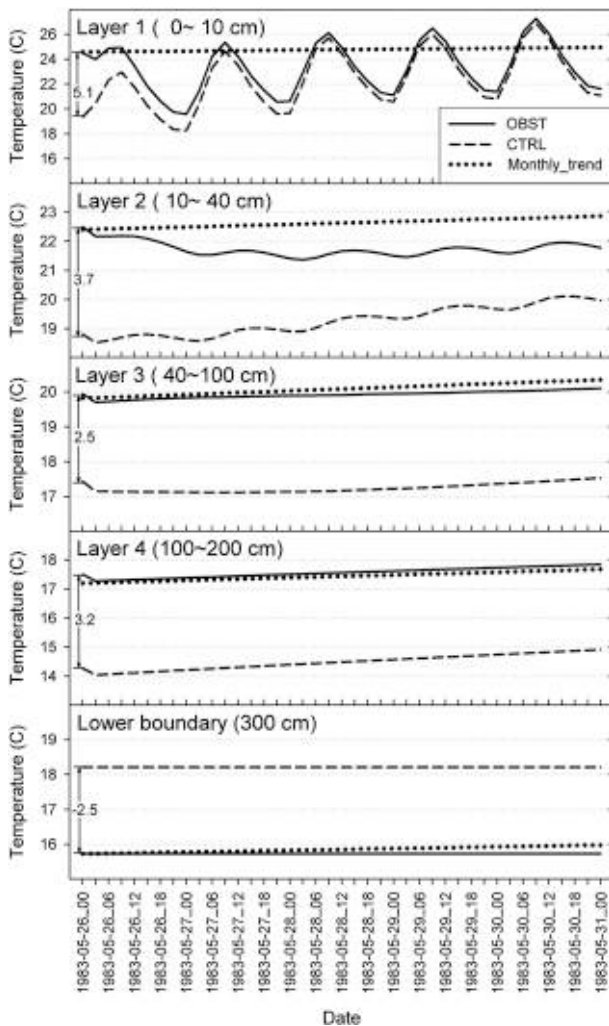


FIG. 10. Average of soil temperatures for stations within the area 25°–35°N, 105°–123°E in the four model soil layers and lower boundary, from OBST (solid), CTRL (dashed), and the observed monthly trend (dotted). Temperature differences (OBST – CTRL) at the initial time of the fine domain are also labeled for each layer.

the difference is largest during the day. The reason for this could be that soil has a larger heat capacity than air, causing lagged influences.

Sensible and latent heat fluxes are associated with surface temperature, evaporation, and evapotranspiration. Thus, they both exhibit a peak in the daytime as the temperature rises and evaporation increases (Figs. 11b,c). There is, in fact, a consistent increase in surface evaporation seen in OBST relative to CTRL (not shown). The differences in these two fluxes between OBST and CTRL experience an increase during the first 6 h due to the introduced soil temperature change.

To investigate the continued impact on the heavy rain that occurred on the fourth simulation day, the spatial distributions of the surface sensible and latent heat

fluxes are analyzed. Taking into account the fact that the features of the soil temperature fields, as well as the SHI discussed above in section 4b, that were introduced at the initial time lasted nearly the entire simulation period, here we focus on the accumulative impacts exhibited in the two heat flux fields. Figure 12 shows the average sensible and latent heat fluxes taken from the 3-hourly model output from the OBST and CTRL experiments and their differences, averaged over the time periods from the initial time of the fine domain through the beginning of the fourth day; that is, simulation hours 15 through 84. This average also reflects the characteristics of the accumulated sensible and latent heat transfer. Over time, both heat fluxes show positive accumulated heat transfer from surface to air over land. A large area of sensible heat transfer exists in the heavy rain area, particularly the area along 30°N and between 110° and 116°E, extending to its northeastern section within the analysis box (Figs. 12a,c). High latent heat accumulated in the rain area as well (Figs. 12b,d). This shows consistency with the findings of Wang and Seaman (1997), who found that total precipitation volume reflects the total amount of latent heating that the model generates. An interesting feature seen in the difference fields (OBST – CTRL; Figs. 12e,f) is an area of increased (positive) energy accumulation of both types of heat transfer over the heavy rain area with an axis approximately parallel to 30°N, while a negative belt surrounds it. The increased sensible energy accumulation seen in OBST is partially associated with the continued soil heating, while the increased latent energy accumulation is associated with the increased surface evaporation as discussed above. Aside from this continuous and significant impact from the soil, there could also be superimposed influences from large-scale atmospheric forcing through the lateral boundaries. Although it is impossible to separate the two impact sources, they work to cancel each other's effect, because the same large-scale atmospheric impact tends to draw the OBST and CTRL simulations closer to one another, while the different soil temperature initializations and lower soil boundary conditions introduce differences. The significance of the impacts of soil temperature seen in the above and following analysis thus implies the importance of this key variable in numerical weather simulations.

This continuous spatial heat flux pattern might lead to dynamical modifications of the atmospheric system as studied by Pielke (2001), Clark and Arritt (1995), and Findell and Eltahir (2003). As will be discussed in section 4f, atmospheric temperature, humidity, low-level airflow, and secondary circulations that enhance convective systems are associated with the changes in the heat fluxes in OBST (Figs. 12e,f).

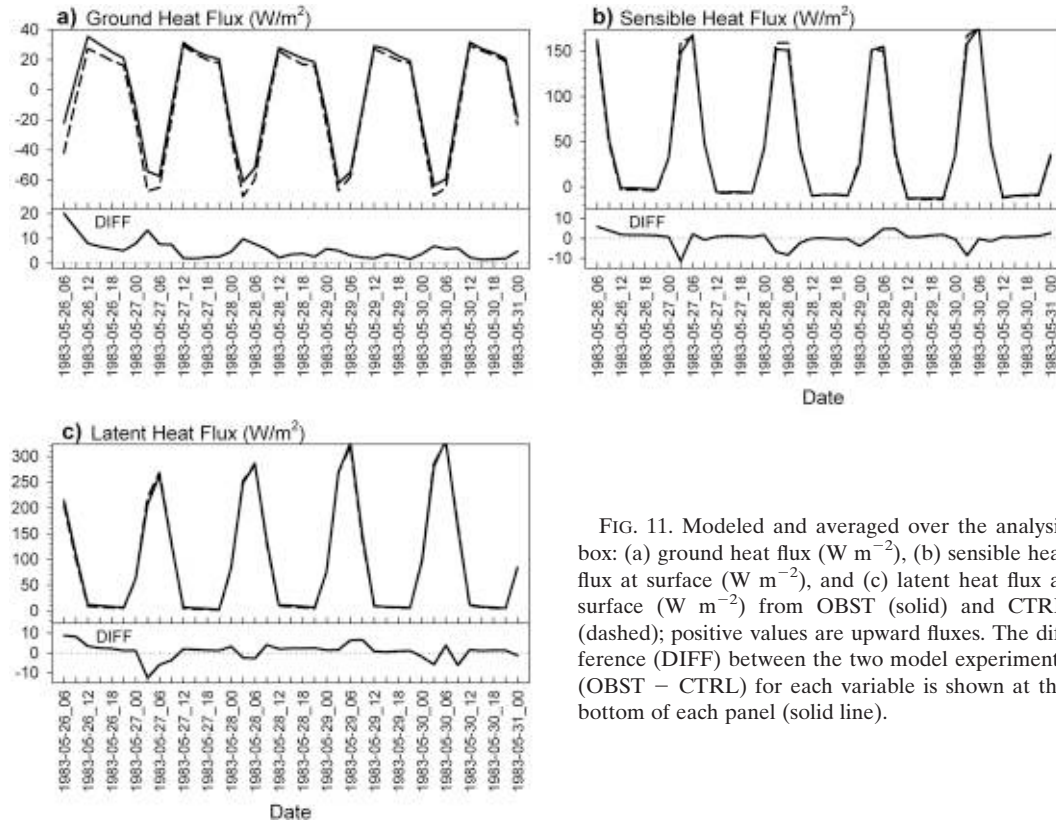


FIG. 11. Modeled and averaged over the analysis box: (a) ground heat flux ($W m^{-2}$), (b) sensible heat flux at surface ($W m^{-2}$), and (c) latent heat flux at surface ($W m^{-2}$) from OBST (solid) and CTRL (dashed); positive values are upward fluxes. The difference (DIFF) between the two model experiments (OBST – CTRL) for each variable is shown at the bottom of each panel (solid line).

e. Impacts on the atmosphere

As the surface fluxes are changed, the state of the low-level atmosphere is necessarily affected. Figure 13 shows the difference between the two experiments for the temperature (T), water vapor mixing ratio (qvp), convective available potential energy (CAPE), and convective stability (STBE), which are averaged over the analysis box on each model level. For the case under study, the soil temperature was increased at the initial time. This causes a direct impact on the air temperature and increases it during the first two days. The air temperature increase in OBST extends from the surface up to about model level 20 (around 800 hPa or 1450 m) during the first day, with a maximum increase of 0.55 K occurring near the surface during the first night (around 2100 UTC; 0500 LT). The magnitude of the change decreased on the second day, though a maximum increase of 0.39 K is seen on the second night.

The difference field of the water vapor mixing ratio (Fig. 13, qvp) indicates the increased water vapor present in the OBST run during the first three days. This is consistent with the increase in surface soil moisture flux (as reflected by latent heat flux) and evaporation as presented above. This excess moisture in OBST, relative to CTRL, accumulated in the air until the third day,

and is consistent with the precipitation increase seen the same day. The increased near-surface temperature and moisture further enhanced the conditions favorable for the development of convective systems, as shown in the difference field of CAPE, which changed in a similar manner as qvp (Fig. 13, CAPE). The analysis of convective stability (Fig. 13, STBE) indicates increased instability at night in OBST, while the daytime stability is comparable to CTRL. The larger differences of STBE at night are consistent with the greater temperature differences in the shallow soil at night. One aspect of STBE that differs from the other three variables is that it experiences a noticeable change between OBST and CTRL for all five days, though there was only a weak decrease on the fourth day (the heavy rain day). This weaker effect is possibly caused by the strong synoptic-scale system that had already formed on this day and which could have masked the change related to the soil temperature.

f. Impacts on low-level atmospheric circulation

As discussed in section 3 regarding the weather pattern on the fourth simulation day, Fig. 14a shows the 850-hPa geopotential height and horizontal wind vectors from OBST, and the difference of geopotential height from

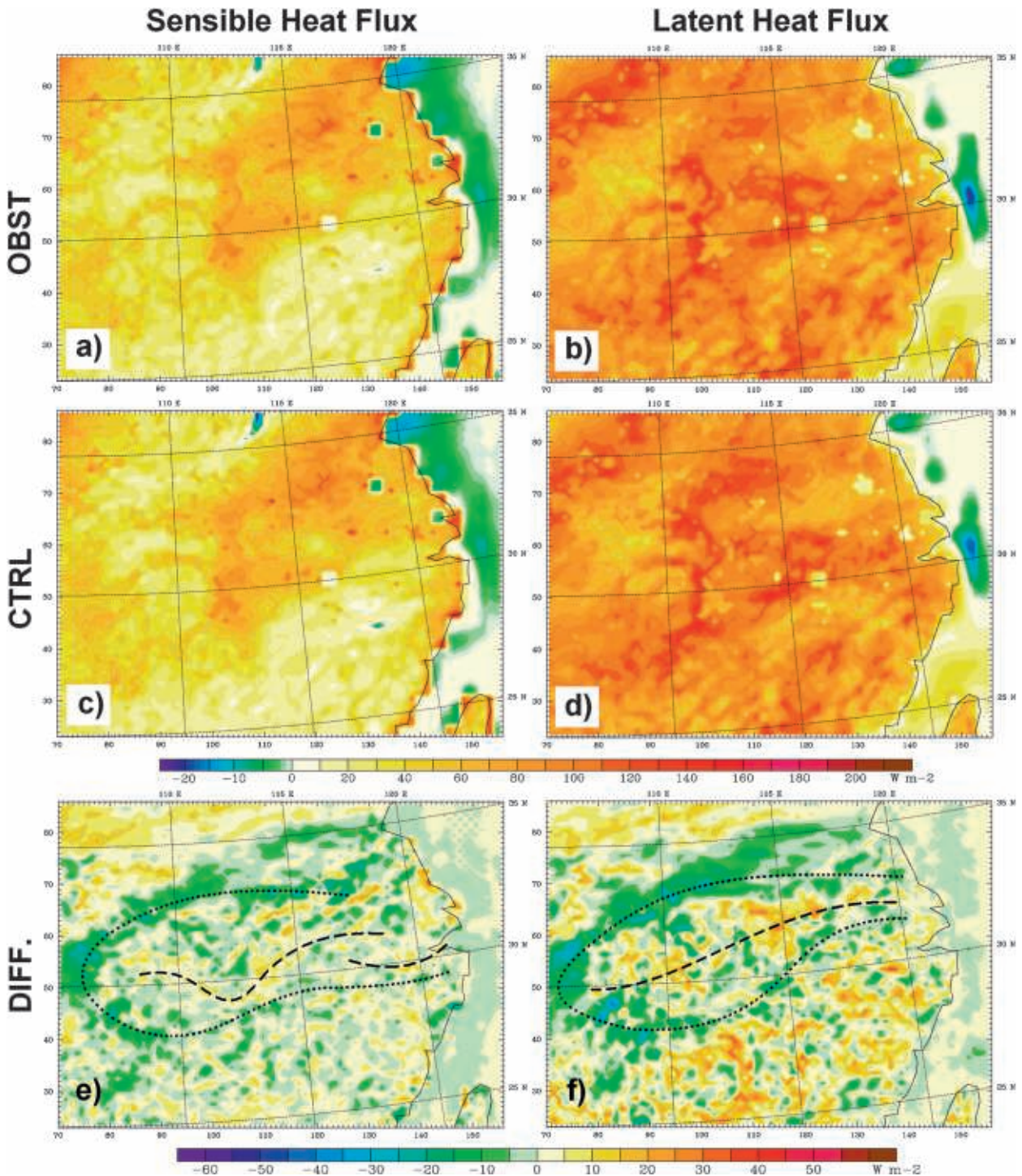


FIG. 12. Average (a),(c),(e) surface sensible heat flux and (b),(d),(f) surface latent heat flux (W m^{-2}) of 3-hourly model output from 0300 UTC 26 to 0000 UTC 29 May 1983 (simulation hour 15 to 84) from experiments (a),(b) OBST and (c),(d) CTRL, and (e),(f) their difference OBST - CTRL. (e),(f) Thick dashed line and dotted line illustrate the axes of positive and negative areas, respectively.

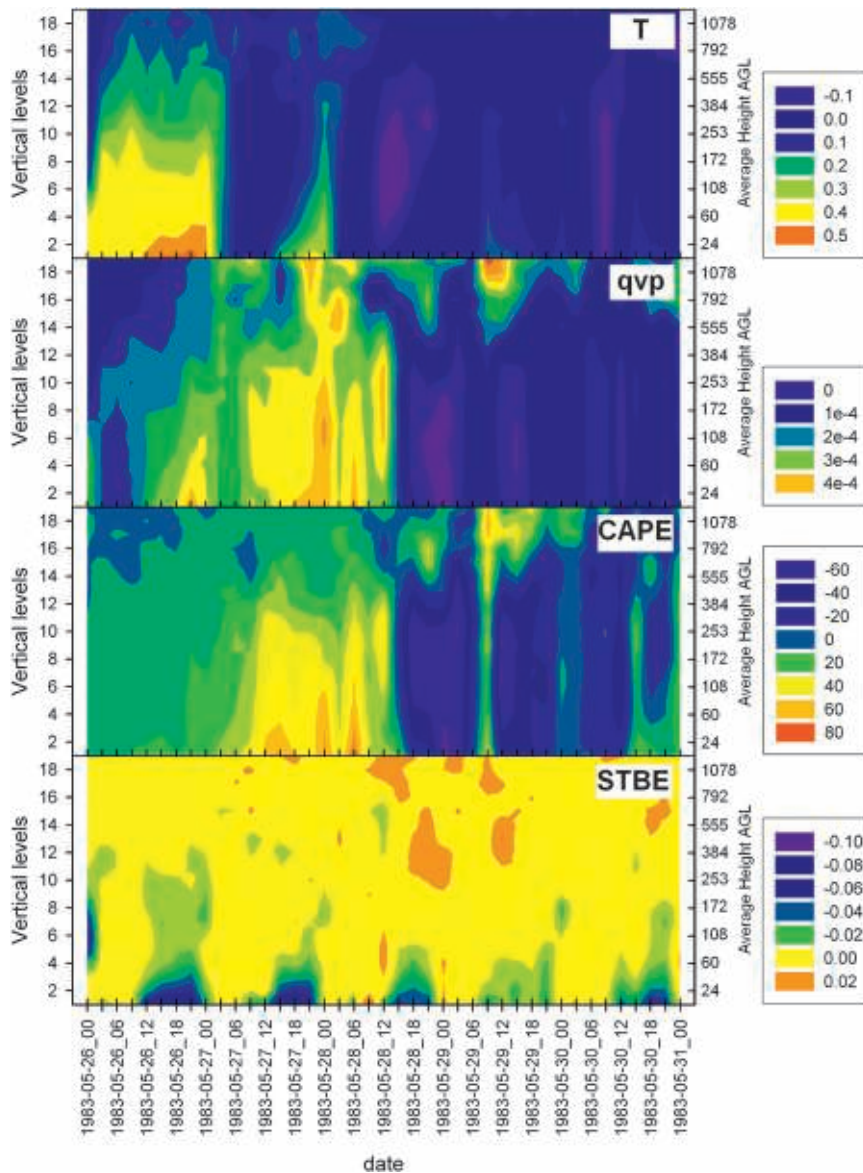


FIG. 13. Difference between the two experiments (OBST – CTRL) for T (K), q_{vp} (g kg^{-1}), CAPE (J kg^{-1}), and STBE (K hPa^{-1}) within the analysis box (see Fig. 1). Average height (m) above ground level (AGL) is also an average within the analysis box.

CTRL, valid at 0000 UTC 29 May 1983. It is shown that the two low pressure systems were in existence at the beginning of the fourth day, approximately parallel to the 30°N parallel, and were accompanied by a southwesterly jet bringing warm air to the rainfall region (cf. Fig. 14b). The entire heavy rain area sees a significant decrease in geopotential height in OBST, while the surrounding areas show increased geopotential height. This significant change in geopotential height also implies an increase in the horizontal pressure gradient, which causes an increase in the jet flow speed as seen in Fig. 14c. Figure 14b shows the 850-hPa temperature field and its difference

between OBST and CTRL. It is shown that for most of the area shown in the window, except for the northeastern and northern parts, the temperature in OBST is generally increased in the warmer areas and decreased in the cooler areas relative to CTRL. This implies an increase in the horizontal temperature gradient and, consequently, increases in the thermal wind. The differenced wind vectors in Fig. 14c show a cyclonic flow in the convective precipitation center shown in Figs. 8b,c (close to the intersection of X1–X2 and Y1–Y2). This cyclonic flow enhancement collocates with an area of decreased geopotential height (Fig. 14a) and increased

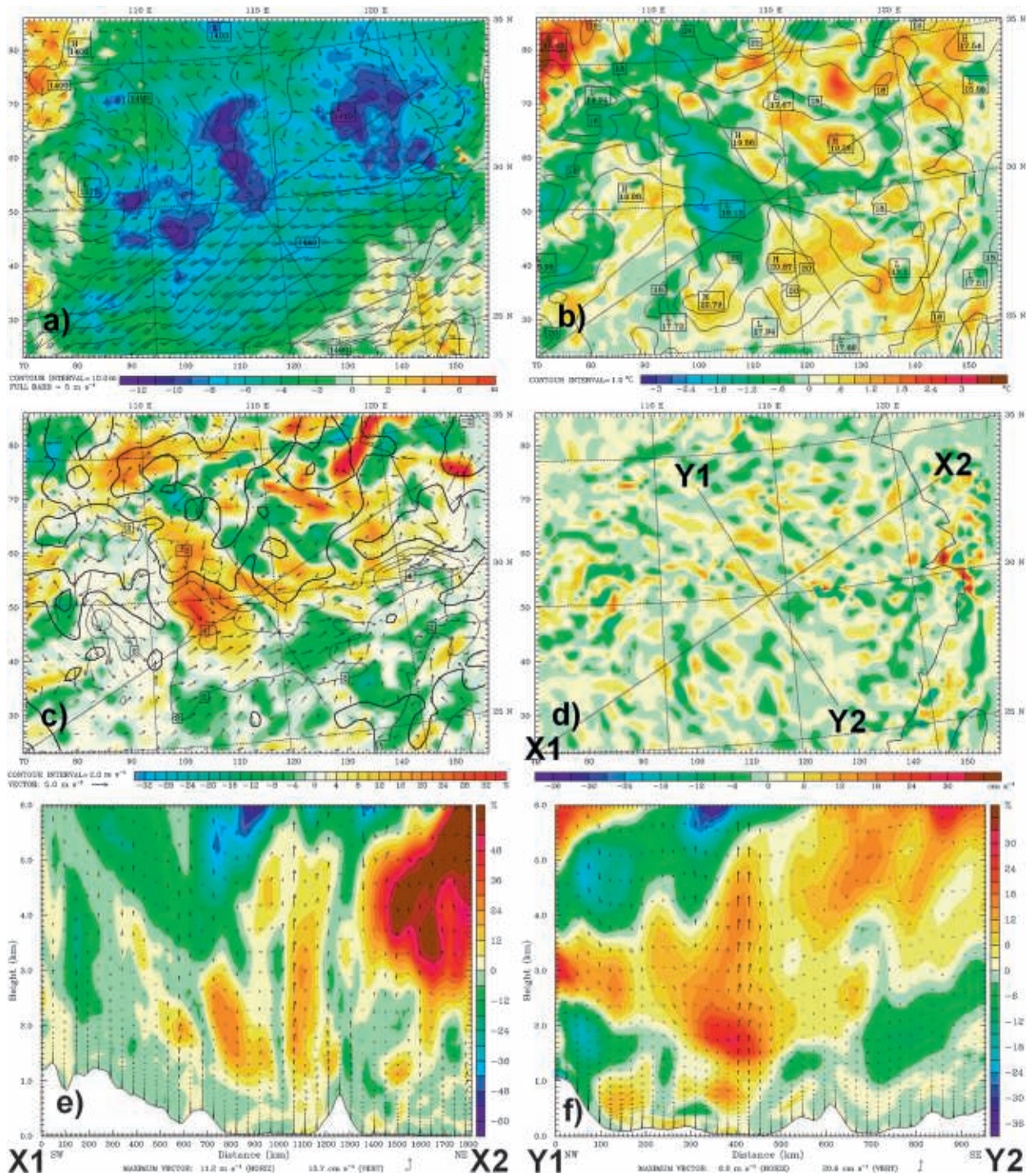


FIG. 14. (a) The 850-hPa geopotential height (contours) and horizontal wind vectors in OBST, and difference of height (shaded); (b) 850-hPa temperature (contours) in OBST and difference of temperature (shaded); (c) differences in relative humidity (shaded), horizontal wind speed (contour), and horizontal wind vectors at 850 hPa; (d) difference in vertical velocity at 850 hPa; (e) difference in relative humidity (shaded) and differenced circulation vectors along cross section X1-X2; (f) same as (e), but along cross section Y1-Y2. All are valid at 0000 UTC 29 May 1983 (simulation hour 84); difference fields are (OBST - CTRL).

humidity (Fig. 14c). As shown in Fig. 14d, as well as Figs. 14e,f, increased upward vertical motion accompanies the increased cyclonic flow and humidity. With the aid of the enhanced cyclonic motion, the moist air is transferred southward along and parallel to Y1–Y2, resulting in more favorable conditions for convective activity. This is further illustrated in Figs. 14e,f, where the differences in the relative humidity and the circulation vectors along the two vertical cross sections are shown. Locations of increased convective motion can be seen in the center of each of the two cross sections. These changes in the humidity and flow fields explain the change in the precipitation field as described in section 4a. Subdividing the 24-h total precipitation into convective and model-resolved components (not shown), it is found that at the two rain centers discussed in section 4a the convective precipitation increased from 72.7 and 40.4 mm to 87.5 and 67.0 mm, and the resolved precipitation increased from 13.6 and 11.7 mm to 19.6 and 35.0 mm, respectively. While both convective and large-scale motions contributed to the total precipitation increase seen in OBST, convective motion played a predominant role in this heavy rain case.

In analyzing convective development and intensity, two thermodynamically related convective parameters, CAPE and 500-hPa lifted index (LI), are often used (e.g., Pielke 2001; Chang and Wetzel 1991). According to Pielke (2001), values of $LI > 0$ are generally associated with no significant cumulus convection; $-4 < LI < 0$ are associated with showers; $-6 < LI < -4$ are associated with thunderstorms; and $LI < -6$ are associated with severe thunderstorms. Figure 15 shows the maximum CAPE (i.e., CAPE for an air parcel with the maximum equivalent potential temperature below 3000 m AGL) and 500 hPa LI for OBST and CTRL, as well as their differences. Although the two parameters began to show changes favorable to convective enhancement from the beginning of the fourth day, only those at 0900 UTC 29 May 1983, when the convective precipitation is strongest (see Fig. 8b), are shown in Fig. 15. It is shown that both the model runs have as large as 2500–3000 $J Kg^{-1}$ CAPE in the heavy rain area; however, OBST shows increased CAPE along the 30°N parallel with increases of 600–1000 $J Kg^{-1}$. Regarding the LI, although both CTRL and OBST exhibit negative values in the heavy rain area, OBST shows even smaller LI and produces a larger area of LI values less than -6 , which is indicative of severe thunderstorms.

The interconnections among the soil heating condition, heat fluxes, atmospheric thermodynamics, weather patterns, and precipitation are consistent with the type 1 events described by F93, as summarized in section 3.

g. Overall results from the six cases

The impacts of changes to the soil temperature initialization and lower boundary condition were found to be similar in the other five cases listed in Table 1 as in the 25 May 1983 case discussed above. To give an objective and quantitative comparison, the changes to the modification of soil temperature and its impact on the surface air temperature and precipitation are emphasized in this subsection. Table 2 lists the initial changes to soil temperatures in the four soil layers and at the lower boundary. In all six cases, the observed soil temperatures are higher than those present in the ERA-40 data. On average, the temperature differences in the four layers are, from top to bottom, 5.6, 4.0, 2.7, and 2.6 K. These increases caused the surface air temperature to increase from the surface up to roughly 20 model levels, as discussed in section 4.5. The maximum increase is found, of course, at the lowest level; it is, on average, 0.5 K on the first day and 0.3 K on the second day.

As discussed in sections 3 and 4b, the lower boundary condition helps in maintaining a strong vertical soil temperature gradient, which contributes to gradients in the shallow layers and indirectly impacts the atmosphere. An average change of -0.7 K in the lower boundary temperature is not as large as in the four soil layers. As mentioned previously, in Noah LSM the lower boundary assumes a constant temperature condition. However, in all six cases, the observed lower boundary temperature follows the seasonal trend and experiences a 3.5-K increase from May to August, which implies that, while the constant temperature lower boundary condition used in the Noah LSM might work for shorter-term weather simulations, it is not appropriate for seasonal and longer-term climate simulations.

The overall impact of the soil temperature on precipitation is analyzed based on ETS and categorical bias. The ETS and bias scores for the 24-h accumulated precipitation on the fourth day of the CTRL and OBST experiments for all six cases are listed in Table 3. This shows that OBST has better skill in predicting precipitation totals at all eight thresholds. At the same time, OBST has improved bias scores for the thresholds of 10–75 mm. For the thresholds of 2 and 5 mm, OBST slightly underestimated the precipitation occurrences compared to CTRL, though both are very close to perfect (with a difference less than 0.1). OBST overestimated the largest threshold more than CTRL did. Overall, both the ETS and bias scores indicate that OBST primarily improved the precipitation prediction at medium to large thresholds, the dominant ranges in the heavy rain cases.

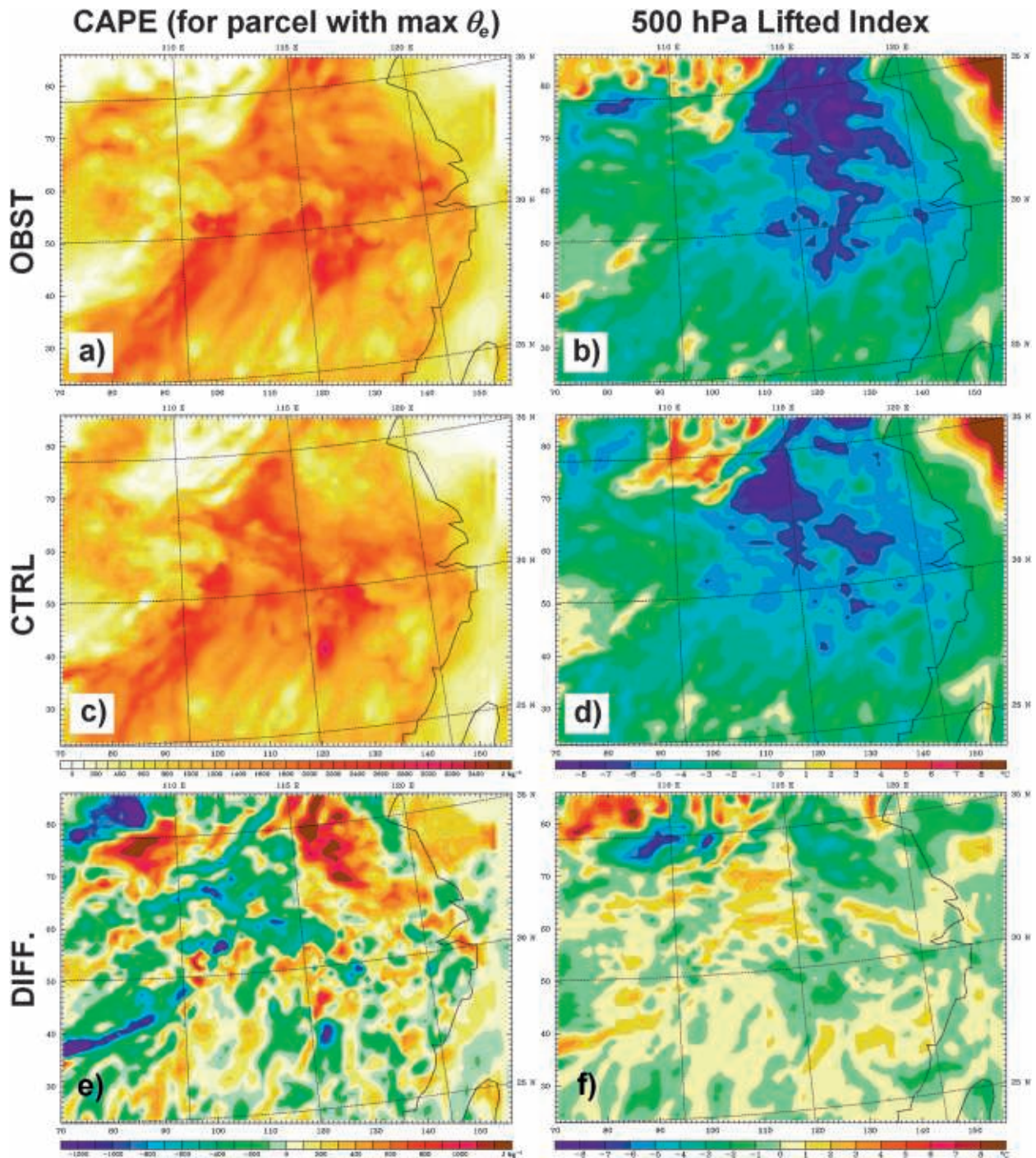


FIG. 15. (a),(c),(e) CAPE for a parcel with maximum equivalent potential temperature below 3000 m above ground level and (b),(d),(f) 500-hPa lifted index from experiments (a),(b) OBST and (c),(d) CTRL, and (e),(f) their difference, valid at 0900 UTC (1700 LT) 29 May 1983.

5. Conclusions and discussion

Because soil temperature influences the ground surface and lower levels of the atmosphere through heat

and moisture fluxes, this influence conceivably extends to larger-scale weather patterns at the local, regional, and global scales, as well as at varying time scales. In the six heavy rain cases studied herein, observed soil

TABLE 2. Initial soil temperature changes in the four soil layers and at the lower boundary, and the corresponding impact on the surface air temperature. All are averaged over the analysis box from the fine domain. Date format as in Table 1.

Case No.	Starting date of fine domains	Initial soil temperature change at each layer (OBST – CTRL; K)					Maximum surface air temperature change (OBST – CTRL; K)	
		1	2	3	4	LB	Day 1	Day 2
1	1980-07-06 0000	5.8	4.0	2.3	2.3	-0.4	0.49	0.21
2	1980-07-17 0000	6.2	4.5	3.2	2.4	0.1	0.49	0.37
3	1980-08-09 0000	5.3	3.9	2.6	1.7	1.0	0.45	0.25
4	1983-05-26 0000	5.1	3.7	2.5	3.2	-2.5	0.55	0.39
5	1983-06-12 0000	5.6	4.0	3.1	3.1	-1.5	0.60	0.27
6	1983-06-27 0000	5.3	3.8	2.7	2.8	-1.0	0.46	0.14
	Average	5.6	4.0	2.7	2.6	-0.7	0.5	0.3

temperatures were used to initialize the land surface model and to provide the lower boundary conditions at the bottom of the modeled soil layer. Through the analysis of various impacts from the introduction of observed soil temperatures, we reach the following conclusions:

- 1) There are large differences in the soil temperatures between the observations and the ERA-40 reanalysis. In addition, there is a sharp contrast between observed temperatures and the assumption about the constancy of the deep soil temperature. A cold bias that decreases with depth is found in ERA-40. On the other hand, the Noah land surface model defaults to a lower boundary soil temperature that is warmer than observed. The utilization of observed soil temperatures introduces a persistent soil heating condition that is favorable to convective development.
- 2) After the soil temperatures are increased on the basis of observations, a consistent increase in ground heat flux is found during the day. Soil temperature changes introduced at the initial time maintain positive values but gradually decrease in magnitude with time. Sensible and latent heat fluxes, as well as the moisture flux, experience an increase during the first 6 h.
- 3) An increase in soil temperature impacts the near-surface air temperature through surface exchange, and moisture through evaporation. During the first two days, an increase in air temperature is seen across the region from the surface up to about 800 hPa (~1450 m). The maximum near-surface air temperature increase is found to be, averaged over all cases, 0.5 K on the first day and 0.3 K on the second day.
- 4) The strength of the low-level jet is affected by the changes described above and also by the consequent changes in horizontal gradients of pressure and thermal fields. Thus, the three-dimensional circulation is affected, in addition to the changes seen in the

humidity and thermal fields and in the locations and intensities of precipitating systems.

- 5) An overall analysis of the six cases indicates that the introduction of observed soil temperature improves the prediction of precipitation.

In this study, the sole change was to the initialized soil temperature. The horizontal boundary conditions were provided by another modeling system (ERA), generated using its own underlying surface conditions. At time scales such as those used in this study, regional weather patterns may not be significantly changed as the lateral boundary conditions are prescribed, though changes to the lower boundary conditions can cause significant impacts to the surface and low-level atmosphere. Although the use of a regional mesoscale model reveals the impacts, surface exchanges, and circulations at small spatial and temporal scales, the impact of a change in the soil on regional weather forecasts may still be limited. A global model would serve as a better tool to investigate the impacts that would be seen from changes made to the soil conditions.

TABLE 3. ETS and BIAS calculated for the 24-h accumulated precipitation on the 4th day of the CTRL and OBST experiments for all six cases, within the analysis box (25°–35°N, 105°–123°E). Gridded precipitation derived from station observations is used for verification. Boldface type highlights the instances where a higher ETS or closer-to-1 bias is found in OBST than in the corresponding CTRL run.

Thresholds (mm)	ETS		Bias	
	CTRL	OBST	CTRL	OBST
2	0.1586	0.1741	0.9119	0.9017
5	0.1569	0.1707	0.9362	0.9179
10	0.1487	0.1672	0.9057	0.9139
20	0.0960	0.1214	0.7676	0.8026
30	0.0620	0.0961	0.6546	0.7121
50	0.0373	0.0856	0.6175	0.6668
75	0.0289	0.0796	0.7412	0.8397
100	-0.0022	0.0575	1.1250	1.2823

Acknowledgments. Great thanks to Jeremy Krieger at the University of Alaska Fairbanks for editing and proof-reading the manuscript. The two anonymous reviewers provided constructive suggestions in the revision of the manuscript. The computational work was primarily conducted at the Arctic Region Supercomputing Center, University of Alaska Fairbanks, and the High Performance Computing Collaboratory, Mississippi State University.

REFERENCES

- Avissar, R., and R. Pielke, 1989: A parameterization of heterogeneous land surfaces for atmospheric numerical models and its impact on regional meteorology. *Mon. Wea. Rev.*, **117**, 2113–2136.
- Betts, A. K., F. Chen, K. E. Mitchell, and Z. Janjic, 1997: Assessment of the land surface and boundary layer models in two operational versions of the NCEP Eta model using FIFE data. *Mon. Wea. Rev.*, **125**, 2896–2916.
- Chang, J.-T., and P. J. Wetzel, 1991: Effects of spatial variations of soil moisture and vegetation on the evolution of a prestorm environment: A numerical case study. *Mon. Wea. Rev.*, **119**, 1368–1390.
- Chen, F., and R. Avissar, 1994: Impact of land-surface moisture variability on local shallow convective cumulus and precipitation in large-scale models. *J. Appl. Meteor.*, **33**, 1382–1401.
- , and J. Dudhia, 2001: Coupling an advanced land surface-hydrology model with the Penn State–NCAR MM5 modeling system. Part I: Model implementation and sensitivity. *Mon. Wea. Rev.*, **129**, 569–585.
- , and Coauthors, 1996: Modeling of land surface evaporation by four schemes and comparison with FIFE observations. *J. Geophys. Res.*, **101** (D3), 7251–7268.
- Cheng, W. Y. Y., and W. J. Steenburgh, 2005: Evaluation of surface sensible weather forecasts by the WRF and the Eta models over the western United States. *Wea. Forecasting*, **20**, 812–821.
- Chudinova, S. M., O. W. Frauenfeld, R. G. Barry, T. Zhang, and V. A. Sorokovikov, 2006: Relationship between air and soil temperature trends and periodicities in the permafrost regions of Russia. *J. Geophys. Res.*, **111**, F02008, doi:10.1029/2005JF000342.
- Clark, C. A., and R. W. Arritt, 1995: Numerical simulations of the effect of soil moisture and vegetation cover on the development of deep convection. *J. Appl. Meteor.*, **34**, 2029–2045.
- Climate Data Office, 1981: Monthly meteorological report of surface observations in China, 1980.01–12. Beijing Meteorological Center, Meteorological Press, 2352 pp.
- , 1984: Monthly meteorological report of surface observations in China, 1980.01–12. Beijing Meteorological Center, Meteorological Press, 2328 pp.
- Cressman, G. P., 1959: An operation objective analysis system. *Mon. Wea. Rev.*, **87**, 367–374.
- Dai, Y., and Coauthors, 2003: The Common Land Model. *Bull. Amer. Meteor. Soc.*, **84**, 1013–1023.
- Deardorff, J. W., 1978: Efficient prediction of ground surface temperature and moisture, with inclusion of a layer of vegetation. *J. Geophys. Res.*, **83**, 1889–1903.
- Diak, G. R., S. Heikkinen, and J. Bates, 1986: The influence of variations in surface treatment on 24-hour forecasts with a limited area model, including a comparison of modeled and satellite-measure surface temperatures. *Mon. Wea. Rev.*, **114**, 215–232.
- Dudhia, J., 1989: Numerical study of convection observed during the winter monsoon experiment using a mesoscale two-dimensional model. *J. Atmos. Sci.*, **46**, 3077–3107.
- Ek, M., and R. H. Cuenca, 1994: Variation in soil parameters: Implications for modeling surface fluxes and atmospheric boundary-layer development. *Bound.-Layer Meteor.*, **70**, 369–383.
- Entekhabi, D., and P. S. Eagleson, 1989: Land surface hydrology parameterization for atmospheric general circulation models including subgrid-scale spatial variability. *J. Climate*, **2**, 816–831.
- Fan, X., 1993: A preliminary analysis of relationship between torrential rain and underlying heat field in mid- and lower-reaches of Yangtze River. *Plateau Meteor.*, **12**, 322–327.
- , and M. Tang, 1996: Structural feature of soil temperature and precipitation and soil heat flux fields of strong earthquakes. *Chin. J. Geophys.*, **39**, 247–261.
- , J. R. Krieger, D. J. Morton, J. Zhang, M. D. Shulski, and A. E. Klenne, 2007: Simulating Beaufort Sea coastal wind events using MM5 and WRF. *Proc. Great Alaska Weather Modeling Symposium*, Fairbanks, AK, National Weather Service, University of Alaska Fairbanks, p. 11.
- Findell, K. L., and E. A. B. Eltahir, 2003: Atmospheric controls on soil moisture-boundary layer interactions. Part II: Feedbacks within the continental United States. *J. Hydrometeor.*, **4**, 570–583.
- Grell, G. A., and D. Devenyi, 2002: A generalized approach to parameterizing convection combining ensemble and data assimilation techniques. *Geophys. Res. Lett.*, **29**, 1693, doi:10.1029/2002GL015311.
- Harris, R. N., and D. S. Chapman, 1997: Borehole temperatures and a baseline for 20th-century global warming estimates. *Science*, **275**, 1618–1621.
- Hong, S.-Y., J. Dudhia, and S.-H. Chen, 2004: A revised approach to ice microphysics process for the bulk parameterization of clouds and precipitation. *Mon. Wea. Rev.*, **132**, 103–120.
- Huang, S., P. Y. Shen, and H. N. Pollack, 1996: Deriving century-long trends of surface temperature change from borehole temperatures. *Geophys. Res. Lett.*, **23**, 257–260.
- Janjic, Z. I., 1996: The surface layer parameterization in the NCEP Eta Model. Preprints, *11th Conf. on Numerical Weather Prediction*, Norfolk, VA, Amer. Meteor. Soc., 354–355.
- , 2002: Nonsingular implementation of the Mellor–Yamada level 2.5 scheme in the NCEP Meso Model. NCEP Office Note, 437, 61 pp.
- Koster, R. D., and Coauthors, 2004: Regions of strong coupling between soil moisture and precipitation. *Science*, **305**, 1138–1140.
- Lachenbruch, A. H., and B. V. Marshall, 1986: Changing climate: Geothermal evidence from permafrost in the Alaskan Arctic. *Science*, **234**, 689–696.
- Mahfouf, J. F., E. Richard, and P. Mascart, 1987: The influence of soil and vegetation on the development of mesoscale circulations. *J. Climate Appl. Meteor.*, **26**, 1483–1495.
- Mintz, Y., 1984: The sensitivity of numerically simulated climates to land surface boundary conditions. *The Global Climate*, J. T. Houghton, Ed., Cambridge University Press, 79–105.
- Mlawer, E. J., S. J. Taubman, P. D. Brwon, M. J. Iacono, and S. A. Clough, 1997: Radiative transfer for inhomogeneous atmosphere: RRTM, a validated correlated-k model for the longwave. *J. Geophys. Res.*, **102** (D14), 16 663–16 682.

- Pan, H. L., and L. Mahrt, 1987: Interaction between soil hydrology and boundary-layer development. *Bound.-Layer Meteor.*, **38**, 185–202.
- Pielke, R. A., Sr., 2001: Influence of the spatial distribution of vegetation and soils on the prediction of cumulus convective rainfall. *Rev. Geophys.*, **39**, 151–177.
- Pollack, H. N., S. Huang, and P.-Y. Shen, 1998: Climate change record in subsurface temperatures: A global perspective. *Science*, **282**, 279–281.
- Skamarock, W. C., J. B. Klemp, J. Dudhia, D. O. Gill, D. M. Barker, W. Wang, and J. G. Powers, 2005: A description of the advanced research WRF Version 2. NCAR Tech. Note 468+STR, 88 pp.
- Sellers, P. J., and Coauthors, 1997: Modeling the exchange of energy, water, and carbon between continents and the atmosphere. *Science*, **275**, doi:10.1126/science.275.5299.502.
- Shukla, J., and Y. Mintz, 1982: Influence of land-surface evapotranspiration on the Earth's climate. *Science*, **215**, doi:10.1126/science.215.4539.1498.
- Sutton, C., T. M. Hamill, and T. T. Warner, 2006: Will perturbing soil moisture improve warm-season ensemble forecasts? A proof of concept. *Mon. Wea. Rev.*, **134**, 3174–3189.
- Tang, M., and J. Zhang, 1994: Seasonal mean soil temperature anomaly field at depth 3.2m and its application in prediction for flood season. *Plateau Meteor.*, **13**, 178–187.
- , Z. Zhao, and Z. Ma, 1997: A summary of flood-season precipitation prediction by using the method of underground information during the recent ten years (1985–1994). *Climatic Environ. Res.*, **2**, 55–60.
- Viterbo, P., and A. C. M. Bejaars, 1995: An improved land surface parameterization scheme in the ECMWF model and its validation. *J. Climate*, **8**, 2816–2748.
- Wang, K., and T. J. Lewis, 1992: Geothermal evidence from Canada for a cold period before recent climatic warming. *Science*, **256**, 1003–1005.
- Wang, W., and N. L. Seaman, 1997: A comparison study of convective parameterization schemes in a mesoscale model. *Mon. Wea. Rev.*, **125**, 252–278.
- Wilks, D., 1995: *Statistical Methods in the Atmospheric Sciences: An Introduction*. Academic Press, 467 pp.
- Xin, J.-S., 1985: Review of ten-year (1975–1984) flood-season precipitation forecasts. *Plateau Meteor.*, **4**, 372–381.
- Xue, Y., F. J. Zeng, K. E. Mitchell, Z. Janjic, and E. Rogers, 2001: The impact of land surface processes on simulation of the U.S. hydrological cycle: A case study of the 1993 flood using the SSIb land surface model in the NCEP Eta regional model. *Mon. Wea. Rev.*, **129**, 2833–2860.
- , P. J. Sellers, J. L. Kinter III, and J. Shukla, 1991: A simplified biosphere model for global climate studies. *J. Climate*, **4**, 345–364.
- Zhang, T., R. G. Barry, D. Gilichinsky, S. S. Bykhovets, V. A. Sorokovikov, and J. Ye, 2001: An amplified signal of climatic change in soil temperatures during the last century at Irkutsk, Russia. *Climatic Change*, **49**, 41–76.
- , M. Serreze, R. G. Barry, D. Gilichinsky, and A. Etringer, 2003: Climate change: Evidence from Russian historical soil temperature measurements. *Geophysical Research Abstracts*, Vol. 5, Abstract 01485. [Available online at <http://www.cosis.net/abstracts/EAE03/01485/EAE03-J-01485.pdf>.]

Copyright of *Monthly Weather Review* is the property of American Meteorological Society and its content may not be copied or emailed to multiple sites or posted to a listserv without the copyright holder's express written permission. However, users may print, download, or email articles for individual use.